CrossMark

J. Fluid Mech. (2019), *vol.* 874, *pp.* 76–101. © Cambridge University Press 2019

This is an Open Access article, distributed under the terms of the Creative Commons Attribution licence (http://creativecommons.org/licenses/by/4.0/), which permits unrestricted re-use, distribution, and reproduction in any medium, provided the original work is properly cited.
doi:10.1017/jfm.2019.432

On low-Prandtl-number convection in an inclined layer of liquid mercury

Oliver Zier[1,2], **Walter Zimmermann**[1] **and Werner Pesch**[1,†]

[1]University of Bayreuth, Theoretische Physik I, Bayreuth 95447, Germany

[2]University Observatory Munich, Scheinerstrasse 1, Munich 81679, Germany

(Received 7 November 2018; revised 22 May 2019; accepted 23 May 2019; first published online 3 July 2019)

This paper reports on a theoretical analysis of convection in an inclined layer of mercury, a common low-Prandtl-number fluid ($Pr = 0.025$). The investigation is based on the standard Oberbeck–Boussinesq equations, which are explored as a function of the inclination angle γ and for Rayleigh numbers R in the vicinity of the convection onset. Along with the conventional Galerkin methods to study convection rolls and their secondary instabilities, we employ direct numerical simulations for fluid layers with quite large aspect ratios. It turns out that, even for small inclination angles $\gamma \lesssim 6°$, the secondary instabilities of the basic rolls lead either to oscillatory three-dimensional patterns or to stationary ones, which appear alternately with increasing γ. Due to the competition of these instabilities the patterns may show a complex dynamics.

Key words: buoyancy-driven instability, nonlinear instability, pattern formation

1. Introduction

Thermal convection in fluids driven by spatial temperature variations has been investigated during the last decades in many theoretical and experimental studies (see e.g. Lappa 2009). The most studied example is Rayleigh–Bénard convection (RBC), where a fluid layer is heated from below and cooled from above. The standard theoretical description is based on the Oberbeck–Boussinesq equations (OBE), which couple the temperature and the velocity field. The main control parameter is the Rayleigh number R, a dimensionless measure of the applied temperature gradient. Theoreticians have extensively analysed the OBE as a model system in order to explore a wide variety of different flow patterns and the transition to turbulence (see e.g. Verma 2018). Besides R, the Prandtl number, Pr, the ratio of the kinematical viscosity, ν, and the thermal diffusivity, κ, plays an important role for the solution manifold of the OBE. To simplify the calculations, one considers often fluid layers of large aspect ratio, i.e. with a height much smaller than the lateral extensions. The layer is then idealized as quasi-infinite and one switches with respect to the planar spatial coordinates into Fourier space. In this way the interpretation of the numerical results becomes much easier, apart from saving a lot of computer time.

For R below the critical Rayleigh number, R_c, the system is in most cases, as also in the present paper, characterized by a uniform heat-conducting basic state. At $R =$

† Email address for correspondence: werner.pesch@uni-bayreuth.de

https://doi.org/10.1017/jfm.2019.432 Published online by Cambridge University Press

R_c this state becomes linearly unstable and RBC sets in frequently in the form of a stationary two-dimensional (2-D) periodic array of counter-rotating convection rolls described by the critical wave vector $\boldsymbol{q} = \boldsymbol{q}_c$. At a sufficiently large R secondary and tertiary bifurcations of the roll patterns appear which lead to three-dimensional (3-D) patterns characterized by the impact of additional Fourier modes in wave vector space and possibly by a periodic time dependence as well.

The construction of the corresponding stability diagrams in the $R - \boldsymbol{q}$ space for $R > R_c$ but not too large R (typically less than $5R_c$), has been promoted since the sixties of the last century in particular by Busse and coworkers (see e.g. Busse 1989). Their general concept, which deploys its full power in Fourier space, has then been permanently extended and refined in many ways (for a general review, see Cross & Hohenberg (1993)). It will be described in the following by the notion bifurcation approach, which still serves as the common starting point to explore new aspects in pattern-forming systems. In particular in gases with $Pr \sim 1$ and not too large R the bifurcation approach has led to a very convincing description of many experiments (for a recent review see, e.g. Bodenschatz, Pesch & Ahlers (2000) and references therein). It is obvious that the bifurcation approach cannot work for turbulent convection at large $R \gtrsim 10^3 R_c$, which in addition is mostly explored in cylindrical geometries. Consequently we will typically not refer to the related papers; for a very recent and quite general discussion including many references we point to the monograph of Verma (2018).

In the present paper we investigate a variant of RBC, namely inclined layer convection (ILC), where the fluid layer is tilted by an angle γ with respect to the horizontal orientation. In contrast to the planar case ($\gamma = 0°$) isotropy is broken by a shear flow, since already in the basic state the fluid flows downwards at the colder upper part of the fluid layer and upwards along the warmer lower one. Thus it is not surprising that ILC has attracted also theoretical studies for decades, mainly for medium and large Pr. In particular we refer to a recent paper for $Pr \sim 1$ and references therein (Subramanian *et al.* 2016) for not too large R, where the bifurcation approach predicts already near R_c as a function of γ, a large variety of different 3-D pattern types in excellent agreement with the experiments.

Motivated by recent papers on ILC with liquid metals, which are characterized by very small $Pr < 0.1$, in the turbulent regime with large $R \gtrsim 10^6$ (Shishkina & Horn 2016; Teimurazov & Frick 2017) we found it attractive to perform a complementary study of this system using the bifurcation approach and direct numerical simulations (DNS) at small R slightly above R_c. For definiteness we have restricted ourselves to mercury with $Pr = 0.025$. First, we found oscillatory secondary instabilities of the basic rolls, well known already for $\gamma = 0°$ (see e.g. Rossby 1969), which lead to time-dependent oscillatory (OS) patterns in the form of waves along the roll axes. On the other hand, already even for small γ competing stationary instabilities have been identified. They lead to specific, so-called subharmonic (SH), 3-D patterns, which are time independent. The detailed analysis of the competition between the OS and the SH patterns sets the frame of the present work.

The paper is organized as follows: after introducing the OBE for ILC in § 2, we sketch the linear instability of the basic state leading to transverse rolls. The critical Rayleigh number R_c and the critical wavenumber q_c are given as functions of γ. Then Galerkin methods are applied to characterize the secondary instabilities of the transverse rolls as a function of γ. In the following section (§ 3) DNS of the OBE for different γ and $R > R_c$ are presented, which confirm the Galerkin stability diagram. It is demonstrated that the arising 3-D patterns, either oscillatory or stationary, can be

https://doi.org/10.1017/jfm.2019.432 Published online by Cambridge University Press

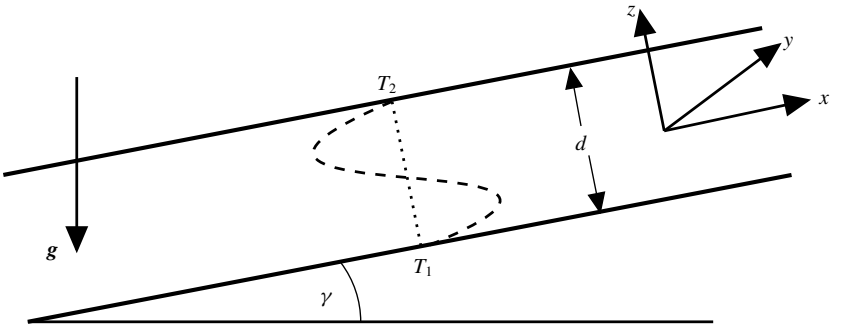

FIGURE 1. Fluid layer of thickness d inclined with an angle γ, heated from below and cooled from above with temperature difference $\Delta T \equiv T_1 - T_2 > 0$. Driven by gravity $\boldsymbol{g}$ the cold fluid flows downwards near the top plate and the hot one flows upwards near the bottom plate leading to a cubic velocity profile across the fluid layer (see (2.2)).

understood in terms of simple analytical expressions. In § 4 a number of complex patterns are discussed, which appear in particular near the various codimension-2 points with respect to γ, where the bifurcation switches from oscillatory to stationary. A short summary of the paper together with perspectives for future work can be found in the conclusions (§ 5). Finally, two appendices are devoted to the numerical methods used in this paper and in particular to a quite detailed discussion of the OS and SH patterns.

2. Roll solutions and their stability

As sketched in figure 1 we consider in this paper ILC as function of the inclination angle γ ($0° \leqslant \gamma \leqslant 90°$). The convection cell is cooled from above (at $z = d/2$) with the fixed temperature $T = T_2$ and heated from below (at $z = -d/2$) with fixed $T = T_1$, where $\Delta T = T_1 - T_2 > 0$. As already indicated before we concentrate on mercury as the working fluid, i.e. exclusively on $Pr = 0.025$. In the following we discuss first the basic equations. Their linear analysis yields the primary instabilities of the basic state in the form of 2-D convection rolls with the wave vector $\boldsymbol{q} = \boldsymbol{q}_c$ at the critical Rayleigh number $R = R_c$. For $R > R_c$ the amplitudes of the rolls continuously grow until at a secondary instability, depending on γ, different 3-D patterns bifurcate.

2.1. *Basic equations*

The interaction of the temperature and velocity field in our system is described by the standard OBE for incompressible fluids. As usual, the OBE are non-dimensionalized using d as the length scale and the vertical diffusion time $t_v = d^2/\kappa$ as the time scale. The velocity $\boldsymbol{u}$ is measured in units of d/t_v, the pressure p in units of $\kappa/(\nu d^2)$. Temperatures are measured in units of $T_s = \nu\kappa/\alpha g d^3$ with α the thermal expansion coefficient. Using a Cartesian coordinate system aligned with the layer (see figure 1), the non-dimensional OBE read as follows:

$$[\partial/\partial t + (\boldsymbol{u}\cdot\boldsymbol{\nabla})]\tilde{T} = \nabla^2\tilde{T} + R\hat{\boldsymbol{z}}\cdot\boldsymbol{u}, \tag{2.1a}$$

$$Pr^{-1}[\partial/\partial t + (\boldsymbol{u}\cdot\boldsymbol{\nabla})]\boldsymbol{u} = \nabla^2\boldsymbol{u} - \frac{\boldsymbol{g}}{g}\tilde{T} - \boldsymbol{\nabla}p, \tag{2.1b}$$

https://doi.org/10.1017/jfm.2019.432 Published online by Cambridge University Press

with the temperature, $\tilde{T}$, and the velocity field, $\boldsymbol{u}$, where $\boldsymbol{\nabla}\cdot\boldsymbol{u}=0$ due to incompressibility. The vector $\boldsymbol{g}=-g(\cos\gamma\hat{\boldsymbol{z}}+\sin\gamma\hat{\boldsymbol{x}})$ describes the effect of gravity with the gravitational constant g. All terms which can be expressed as gradients are included in the pressure term $-\boldsymbol{\nabla}p$. Equations (2.1) are characterized by the angle of inclination γ along with the two non-dimensional parameters, the Rayleigh number $R=\Delta T/T_s$ and the Prandtl number $Pr=\nu/\kappa$.

In line with previous theoretical investigations of ILC on the basis of the bifurcation approach in the literature (see in particular Clever & Busse (1977), Busse & Clever (1992)) we use periodic boundary conditions with respect to x and y. At the vertical boundaries $z=\pm1/2$ (in dimensionless units) the temperatures are kept fixed and the velocity is assumed to vanish (rigid boundary conditions). Equations (2.1) then admit primary (basic) solutions (denoted with subscript 0) of a linear temperature profile $\tilde{T}_0(z)$ and cubic shear velocity profile $\boldsymbol{U}_0(z)$,

$$\tilde{T}_0(z)=R\left[\frac{T_1+T_2}{2\Delta T}-z\right],\quad \boldsymbol{U}_0(z)=\hat{\boldsymbol{x}}\sin\gamma R\frac{z}{6}\left[z^2-\frac{1}{4}\right]\equiv\hat{\boldsymbol{x}}\sin\gamma RU_0^x(z). \tag{2.2a,b}$$

In the presence of convection $\tilde{T}_0$ is modified by $\theta(x,y,z,t)$ and $\boldsymbol{U}_0$ by $\boldsymbol{v}$ as follows:

$$\tilde{T}(\boldsymbol{x},z,t)=\tilde{T}_0(z)+\theta(\boldsymbol{x},z,t),\quad \boldsymbol{u}(\boldsymbol{x},z,t)=\boldsymbol{U}_0+\boldsymbol{v}(\boldsymbol{x},z,t),\quad \boldsymbol{x}=(x,y), \tag{2.3a,b}$$

which fulfil the boundary conditions $\theta(z=\pm1/2)=\boldsymbol{v}(z=\pm1/2)=0$.

It is convenient to map the solenoidal velocity field $\boldsymbol{v}$ in (2.3*b*) by the well-known poloidal–toroidal decomposition to two scalar velocity functions f, $\Phi(\boldsymbol{x},z,t)$ and a correction $\boldsymbol{U}(z,t)=(U_x,U_y,0)$ of $\boldsymbol{U}_0(z)$ (2.2*b*),

$$\boldsymbol{v}(x,y,z,t)=\boldsymbol{\nabla}\times(\boldsymbol{\nabla}\times f\hat{\boldsymbol{z}})+\boldsymbol{\nabla}\times\Phi\hat{\boldsymbol{z}}+\boldsymbol{U}(z,t)\equiv\boldsymbol{\chi}f+\boldsymbol{\eta}\Phi+\boldsymbol{U}(z,t). \tag{2.4}$$

The equations for f, Φ are obtained by inserting $\boldsymbol{u}$ (2.3*b*) with $\boldsymbol{v}$ (2.4) into (2.1*b*) followed by the application of the operators $\boldsymbol{\chi}$, $\boldsymbol{\eta}$. The equation for θ results from inserting the ansatz for $\tilde{T}$ (2.3*a*) into (2.1*a*). The explicit expressions for the linear equations are thus given as

$$\partial_t\theta=-R\Delta_2 f+\nabla^2\theta-R\sin\gamma\,(U_0^x(z)\partial_x)\theta, \tag{2.5a}$$

$$\frac{1}{Pr}\partial_t\nabla^2\Delta_2 f=\nabla^4\Delta_2 f-\cos\gamma\,\Delta_2\theta+\sin\gamma\,\partial_x\partial_z\theta-\frac{1}{Pr}\sin\gamma R\mathcal{F}[U_0^x]f, \tag{2.5b}$$

$$\frac{1}{Pr}\partial_t\Delta_2\Phi=\nabla^2\Delta_2\Phi+\sin\gamma\,\partial_y\theta-\frac{1}{Pr}[(U_0\partial_x)\Delta_2\Phi+([\partial_z U_0]\partial_y)\Delta_2 f], \tag{2.5c}$$

with the operators $\Delta_2=(\partial_{xx}+\partial_{yy})$ and $\mathcal{F}[U_0^x]\equiv[U_0^x(z)\nabla^2-\partial_{zz}^2U_0^x(z)]\partial_x\Delta_2$. It should be noted that the pressure has dropped out in (2.5).

For the following, a compact symbolic representation of the OBE (2.1) transcribed to $\theta, f, \Phi, \boldsymbol{U}$ using (2.3) and (2.4) is convenient,

$$\widehat{\mathcal{C}}\frac{\partial}{\partial t}\widehat{\boldsymbol{V}}(\boldsymbol{x},z,t)=\widehat{\mathcal{L}}\,\widehat{\boldsymbol{V}}(\boldsymbol{x},z,t)+\widehat{\boldsymbol{N}}[\boldsymbol{v}+\boldsymbol{U},\widehat{\boldsymbol{V}}], \tag{2.6}$$

with $\boldsymbol{x}=(x,y)$ and the symbolic vector $\widehat{\boldsymbol{V}}=[\theta,f,\Phi]^{\mathrm{T}}$. The linear operators $\widehat{\mathcal{C}}$, $\widehat{\mathcal{L}}$ are given in (2.5). The symbol $\widehat{\boldsymbol{N}}$ stands for the nonlinear terms which consist of quadratic

https://doi.org/10.1017/jfm.2019.432 Published online by Cambridge University Press

forms in θ, f, Φ and $\boldsymbol{U}$ and their spatial derivatives. The components of $\widehat{\boldsymbol{N}}$ are given as

$$\widehat{N}_\theta = (\boldsymbol{v}\cdot\boldsymbol{\nabla})\theta, \quad \widehat{N}_{(f;\Phi)} = (\boldsymbol{\chi};\eta)[(\boldsymbol{v}\cdot\boldsymbol{\nabla})(\boldsymbol{\chi} f + \eta\Phi)]. \tag{2.7a,b}$$

The evolution equation for the secondary mean flow $\boldsymbol{U}(z,t)$ results from averaging the velocity equation (2.1*b*) over the x–y plane, leading to

$$\frac{1}{Pr}\frac{\partial \boldsymbol{U}(z,t)}{\partial t} = -\frac{1}{Pr}\frac{\partial \overline{(v_z \boldsymbol{v})}}{\partial z} + \frac{\partial^2 \boldsymbol{U}}{\partial z^2} + \sin\gamma\,\overline{\theta}\,\hat{\boldsymbol{x}} - (\partial_x, \partial_y, 0)(P_x(t)x + P_y(t)y), \tag{2.8}$$

where the overbar indicates the horizontal average. Note that (2.8) contains a special pressure term first proposed in Busse & Clever (2000) in a different context. The functions $P_x(t), P_y(t)$ have to be chosen to guarantee mass conservation, i.e. $\int \mathrm{d}z \boldsymbol{U}(z) = 0$; non-zero $P_{x,y}$, however, appear only in the DNS of complex patterns in § 4.

In general (2.6) is solved with respect to x, y on a rectangle with the lateral extensions L_x, L_y using periodic boundary condition, i.e. $\widehat{\boldsymbol{V}}(x,y,z) = \widehat{\boldsymbol{V}}(x+L_x, y+L_y, z)$ holds. That is guaranteed by using the following discrete Fourier representation:

$$\widehat{\boldsymbol{V}}(\boldsymbol{x},z,t) = \sum_{\boldsymbol{q}} \mathrm{e}^{\mathrm{i}\boldsymbol{q}\cdot\boldsymbol{x}} \boldsymbol{V}(\boldsymbol{q},z,t) \quad \text{with } \boldsymbol{q} = (k\,\Delta q_x, l\Delta q_y);\ -N/2 \leqslant (k,l) \leqslant N/2, \tag{2.9}$$

where $\Delta q_x = 2\pi/L_x$, $\Delta q_y = 2\pi/L_y$. Thus the simulations run in Fourier space on a 2-D grid of N^2 wave vectors. Since $\boldsymbol{V}$ is real the condition $\boldsymbol{V}(\boldsymbol{q},z,t) = \boldsymbol{V}(-\boldsymbol{q},z,t)^*$ has to be fulfilled.

The boundary conditions like $\theta(z=\pm 1/2) = 0$ are automatically satisfied by the use of truncated Galerkin expansions with respect to z. For example, θ is represented by the ansatz

$$\theta(\boldsymbol{x},z,t) = \sum_{m=1}^{M} S_m(z)\vartheta_m(\boldsymbol{x},t); \quad S_m(z) = \sin(m\pi(z+1/2)), \tag{2.10}$$

which is analogously used also for Φ and $\boldsymbol{U}(z,t)$. The rigid boundary conditions for $\boldsymbol{v}$ require that f has to be expanded in terms of the Chandrasekhar functions $C_m(z)$ (Chandrasekhar 1961). Consequently our OBE are finally mapped to a system of ordinary differential equations in time for the Fourier coefficients of $\vartheta_m(\boldsymbol{x},t)$ and the corresponding ones for f, Φ and $\boldsymbol{U}$. The Galerkin expansions with respect to the z-direction (see e.g. (2.10)) have been always truncated at $M = 8$ modes. In line with the Appendix of Subramanian *et al.* (2016) we have tested by increasing M that the numbers given in the present paper are afflicted with a relative error of less than 0.1 %.

2.2. *Linear stability analysis of the basic state*

The primary convection instability of the basic state corresponds to exponentially growing solutions in time of the linear equations (2.5). Thus, using the common convection roll ansatz $\widehat{\boldsymbol{V}}(\boldsymbol{x},z,t) = \mathrm{e}^{\sigma t}\mathrm{e}^{\mathrm{i}\boldsymbol{q}\cdot\boldsymbol{x}}\tilde{\boldsymbol{V}}(\boldsymbol{q},z,R)$ in (2.6) with $\widehat{\boldsymbol{N}} = 0$, we arrive from (2.6) at the following linear eigenvalue problem for σ:

$$\sigma\mathcal{C}(\boldsymbol{q},\partial_z)\tilde{\boldsymbol{V}}(\boldsymbol{q},z;R) = \mathcal{L}\tilde{\boldsymbol{V}}(\boldsymbol{q},z;R), \tag{2.11}$$

where the operators $\mathcal{C}$, $\mathcal{L}(\boldsymbol{q},\partial_z)$, etc. in Fourier space derive from the corresponding ones in position space (see (2.5)) via the transformation $\partial_{\boldsymbol{x}} \to \mathrm{i}\boldsymbol{q}$. As indicated before (see e.g. (2.10)) the z-dependence of $\tilde{\boldsymbol{V}}(\boldsymbol{q},z;R)$ is captured by Galerkin expansions with $M = 8$ modes. It turns out that it is sufficient to confine the analysis to the θ, f equations in (2.5). Thus, one arrives finally at an algebraic linear eigenvalue problem

https://doi.org/10.1017/jfm.2019.432 Published online by Cambridge University Press

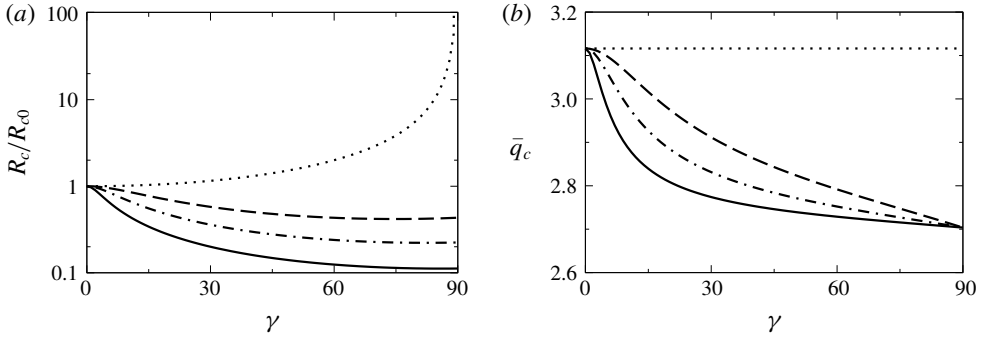

FIGURE 2. Linear instability of the ILC basic state for $Pr = 0.025$ (see (2.2)) as a function of the inclination angle γ with respect to rolls of wave vector $\boldsymbol{q} = (q_x, q_y) = \bar{q}_c(\gamma, \psi)(\cos\psi, \sin\psi)$ at $R = \bar{R}_c(\gamma, \psi)$. (*a*) Reduced critical Rayleigh number $\bar{R}_c(\gamma, \psi)/R_{c0}$ (logarithmic scale) with $R_{c0} = 1707.8$. (*b*) Critical wavenumber $\bar{q}_c(\gamma, \psi)$. The solid lines correspond to the transverse rolls, where $\bar{R}_c(\gamma, \psi = 0°)$ is minimal. For the other ψ the following line styles are used: dotted for longitudinal rolls ($\psi = 90°$), dashed for $\psi = 75°$ and dash-dotted for $\psi = 60°$.

of dimension $2M$ in the Fourier–Galerkin space, which is analysed using a standard linear-algebra package, LAPACK. Let $\sigma_{max}(R, Pr, \gamma, \boldsymbol{q})$ define the eigenvalue σ with the largest real part in (2.11); then rolls become unstable when $\sigma_{max}(R, Pr, \gamma, \boldsymbol{q})$ crosses zero. For each $\boldsymbol{q}$ we have to determine the smallest solution $R = R_0(\boldsymbol{q})$ of $Re[\sigma_{max}(\boldsymbol{q})] = 0$ (the fixed parameters Pr, γ are suppressed for the moment). The minimum of $R_0(\boldsymbol{q})$ with respect to $\boldsymbol{q}$ defines the critical wave vector $\boldsymbol{q}_c$ and the critical Rayleigh number $R_c = R_0(\boldsymbol{q}_c)$ at which the basic state becomes unstable against convection rolls with wave vector $\boldsymbol{q}_c$. The bifurcation turns out to be always stationary since $Im[\sigma_{max}(R_c, \boldsymbol{q}_c)] \equiv 0$; otherwise one would speak of an oscillatory bifurcation.

It is convenient to parameterize the orientation of a wave vector $\boldsymbol{q}$ in the x–y plane as $\boldsymbol{q} = \bar{q}(\psi)(\cos\psi, \sin\psi)$. Thus we obtain from $Re[\sigma_{max}] = 0$ the critical data $\bar{q}_c(\psi)$, $\bar{R}_c(\psi)$, which depend on γ. At $\gamma = 0°$ we deal with the standard isotropic RBC, where $\bar{q}_c = q_{c0} = 3.116$ and $\bar{R}_c = R_{c0} = 1707.8$ depend neither on ψ nor on Pr.

In figure 2 one finds representative plots of $\bar{q}_c(\gamma, \psi)$ and $\bar{R}_c(\gamma, \psi)$ as function of γ for different ψ at fixed $Pr = 0.025$. One sees that the convection onset is realized by transverse rolls ($\psi = 0°$) for all γ. This is in contrast to the case of medium Pr. There exists a so-called codimension-2 point, γ_{c2}, such that for $0° < \gamma < \gamma_{c2}$ longitudinal rolls with $\psi = 90°$ bifurcate at onset in contrast to transverse rolls ($\psi = 0°$) for $\gamma > \gamma_{c2}$. With decreasing Prandtl number γ_{c2} moves continuously downwards to zero until for $Pr < 0.264$ indeed only transverse rolls bifurcate at onset for $0° < \gamma < 90°$ (for a detailed discussion, see appendix C in Subramanian *et al.* (2016)). It is further evident, that $R_c(\gamma) = \bar{R}_c(\gamma, \psi = 0°)$ decreases strongly with γ. This applies also to the critical wavenumber $q_c(\gamma) = \bar{q}_c(\gamma, \psi = 0°)$, although the decay is much weaker.

To measure directly the relative distance of R from R_c we use in the following two definitions of a reduced control parameters, either ϵ or ϵ_0, which are defined as

$$\epsilon = \frac{R - R_c(\gamma)}{R_c(\gamma)}; \quad \epsilon_0 = \frac{R - R_{c0}}{R_{c0}}; \quad R_{c0} \equiv R_c(\gamma = 0°) = 1707.8. \qquad (2.12a\text{–}c)$$

https://doi.org/10.1017/jfm.2019.432 Published online by Cambridge University Press

γ (deg.)	q_c	R_c	ϵ_0	γ (deg.)	q_c	R_c	ϵ_0
0	3.1162	1707.8	0	50	2.7396	236.06	−0.8618
10	2.8894	777.22	−0.5449	60	2.7288	212.45	−0.8756
20	2.8091	468.23	−0.7258	70	2.7197	198.61	−0.8837
30	2.7740	341.32	−0.8001	80	2.7116	191.91	−0.8876
40	2.7536	274.90	−0.8390	90	2.7037	191.27	−0.8880

TABLE 1. Critical Rayleigh number $R_c(\gamma)$ and critical wavenumber $q_c(\gamma)$ of transverse rolls together with $\epsilon_0 = (R_c(\gamma) - R_{c0})/R_{c0}$ (2.12) for increasing γ.

Selected numerical values of R_c and q_c as functions of γ, which correspond to the bold lower curves in figure 2, are listed in table 1. When gradually increasing R beyond $R_c(\gamma)$ finite-amplitude transverse roll patterns with wavenumber $q_c(\gamma)$ develop. Their stability analysis will be discussed in the following subsection.

2.3. *Secondary instabilities of transverse rolls*

The finite-amplitude stationary transverse rolls which develop with wave vector $\boldsymbol{q}_c(\gamma) = (q_c(\gamma), 0)$ for $R > R_c(\gamma)$ (see table 1) are represented as a special case of (2.9) as follows:

$$\widehat{\boldsymbol{V}}_r(x, z) = \sum_{k=-N_r/2}^{N_r/2} \mathrm{e}^{\mathrm{i}kq_c x} \boldsymbol{V}_r(kq_c, z), \tag{2.13}$$

where a cutoff $N_r = 10$ was found to be sufficient in the present context. With respect to z, we introduce again a Galerkin expansion (see (2.10)) of the $(N_r + 1)$ Fourier coefficients $\boldsymbol{V}_r(kq_c, z)$. Thus we arrive at $(3M)N_r$ coupled nonlinear algebraic equations for the expansion coefficients in the resulting Fourier–Galerkin representation. Furthermore, the Galerkin expansion of the mean flow $\boldsymbol{U}$ using sine functions leads to $2M$ additional equations. The whole system is then solved by Newton–Raphson methods. Non-trivial solutions exist only for $R > R_c(\boldsymbol{q})$. Thus the bifurcation to transverse rolls is continuous (supercritical). To examine the linear stability of a transverse roll solution we linearize our general equations about $\widehat{\boldsymbol{V}}_r(x, z)$ with respect to an infinitesimal perturbation $\delta\widehat{\boldsymbol{V}}_r$ in the form of the standard Floquet ansatz

$$\delta\widehat{\boldsymbol{V}}_r(\boldsymbol{x}, z, t) = \mathrm{e}^{\Sigma t}\mathrm{e}^{\mathrm{i}\boldsymbol{s}\cdot\boldsymbol{x}} \sum_{k=-N/2}^{k=N/2} \mathrm{e}^{\mathrm{i}kq_c x} \delta\boldsymbol{V}_r(kq_c, z). \tag{2.14}$$

Thus, we arrive at a linear eigenvalue problem for the eigenvalues $\Sigma(\boldsymbol{s}, q_c, R)$ at fixed R; the γ-dependence will be typically suppressed in the following. The eigenvalue Σ with the largest real part, $\Sigma_0(\boldsymbol{s}, q_c, R)$, determines the growth rate of the perturbation $\delta\widehat{\boldsymbol{V}}_r$ in (2.14). The condition $Re[\Sigma_0(\boldsymbol{s}, q_c, R)] = 0$ indicates thus a secondary instability of the transverse rolls with wavenumber q_c at $R = R_0(\boldsymbol{s}, q_c)$. The minimum of $R_0(\boldsymbol{s}, q_c)$ with respect to $\boldsymbol{s}$ gives the Floquet vector $\boldsymbol{s}_{in}(q_c)$ of the most effective perturbation $\delta\widehat{\boldsymbol{V}}_r(\boldsymbol{x}, z, t)$ driving the instability of the transverse rolls at $R_{in}(q_c) = R_0(\boldsymbol{s}_{in}, q_c)$, where the index *in* points to secondary instability. The frequency at onset is determined by $\omega_{in} = \mathrm{Im}[\Sigma_0(\boldsymbol{s}_{in}, q_c, R_{in})]$. For $|\omega_{in}| > 0$ the secondary instability is oscillatory, otherwise stationary. The corresponding Fourier

https://doi.org/10.1017/jfm.2019.432 Published online by Cambridge University Press

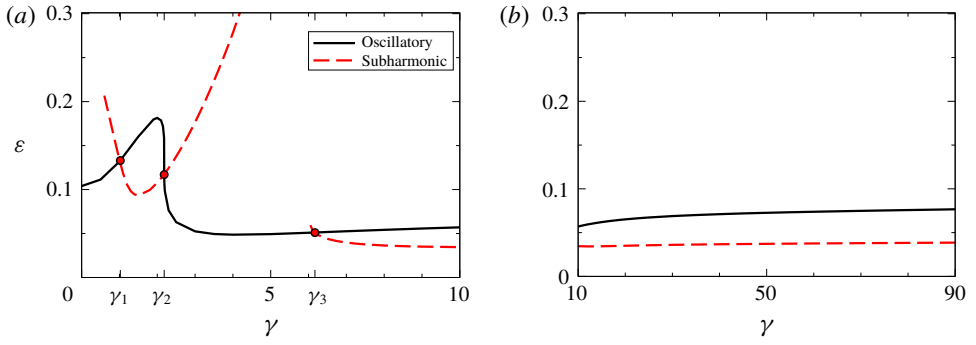

FIGURE 3. (Colour online) Stability diagram of transverse rolls for $Pr = 0.025$ with $0° \leqslant \gamma \leqslant 10°$ (*a*) and $10° \leqslant \gamma \leqslant 90°$ (*b*). The basic state in (2.2), stable for $\epsilon < 0$ (2.12), becomes unstable against the transverse rolls for $\epsilon > 0$. These are stable below the lowest of the two lines, which determine either the OS instability at $\epsilon = \epsilon_{OS}$ (solid line) or the SH instability at $\epsilon = \epsilon_{SH}$ (dashed). The three crossing points of the two curves define the codimension-2 points $\gamma_{1,2,3}$.

coefficient $\delta \boldsymbol{V}_r(kq_c, z)$ in (2.14) takes its maximum for a value $k = k_{max}$ with $|k_{max}| \leqslant 1$. The most effective destabilizing modes are thus characterized by the wave vectors $\boldsymbol{q}_{in} = (k_{max}\, q_c,\, 0) + \boldsymbol{s}_{in}$. In the present system we find a twofold degeneracy of the eigenvalues $\sigma_0(\boldsymbol{s}_{in}, q_c, R)$, since they take the same values for $\boldsymbol{s} = (s_x, \pm s_y^{in})$. Depending on γ we find either oscillatory or stationary secondary instabilities. For the first one, with $k_{max} = 1$, the dominant Fourier coefficients in (2.14) belong to the wave vectors $\boldsymbol{q}_{2,3} = (q_c,\, \pm s_y^{OS})$, while for the second one with $k_{max} = 0$ the dominant modes belong to $\boldsymbol{q}_{2,3} = (q_c/2,\, \pm s_y^{SH})$. In figure 3 we show the whole secondary-bifurcation diagram in the γ–ϵ plane for $Pr = 0.025$. The well-known OS instability at $\gamma = 0°$ remains dominant up to the first codimension-2 point $\gamma_1 = 1.023°$. Then the stationary SH instability takes over in the interval $\gamma_1 < \gamma < \gamma_2 = 2.183°$ with the second codimension-2 point γ_2. Up to the third codimension-2 point $\gamma_3 = 6.169°$ again the OS instability dominates, which is then finally replaced again by the subharmonic one for $\gamma_3 < \gamma < 90°$. The detailed data for the two instabilities are contained in table 2 for a representative set of inclination angles γ.

3. Regular OS and SH patterns

According to the previous section (see table 2) one finds as a function of γ either the OS secondary instability of transverse rolls at $\epsilon_{in} = \epsilon_{OS}$ or the SH instability at $\epsilon_{in} = \epsilon_{SH}$. For $\epsilon \gtrsim \epsilon_{in}$ the amplitudes of the corresponding destabilizing modes, characterized by the Floquet vectors $\boldsymbol{s}_{in}$, start growing exponentially. They are found to saturate eventually into steady regular 3-D patterns in the nonlinear regime with finite complex amplitudes. As obvious from the stability diagram in figure 3 and the discussion before, the most spectacular γ-regime is found for $\gamma \lesssim \gamma_3 = 6.169°$, on which we will mainly concentrate in this paper. In the whole interval $\gamma_3 < \gamma \leqq 90°$, where the SH instability prevails, it is sufficient to consider only a few representative examples.

The nonlinear evolution of the system for $\epsilon > \epsilon_{in}$ is studied in the present section by DNS of the OBE. In the x–y plane we use periodic boundary conditions on a rectangle of area $L_x \times L_y$ and consequently the calculations are performed in Fourier

https://doi.org/10.1017/jfm.2019.432 Published online by Cambridge University Press

https://doi.org/10.1017/jfm.2019.432 Published online by Cambridge University Press

Oscillatory instability (C1)					Subharmonic instability (C2)				Codimension-2 points (C3)				
γ (deg.)	ϵ_{OS}	s_y^{OS}	ω_0	q_c	γ (deg.)	ϵ_{SH}	s_y^{SH}	q_c	γ (deg.)	ϵ_{in}	s_y^{OS}	ω	s_y^{SH}
0	0.104	2.171	1.394	3.116	1	0.139	1.640	3.106	1.023	0.133	2.070	1.314	1.672
0.5	0.111	2.147	1.376	3.114	1.5	0.093	2.241	3.094	2.183	0.117	1.898	0.662	2.468
1.0	0.132	2.075	1.318	3.106	2.0	0.108	2.436	3.080	6.169	0.051	1.923	0.402	1.621
1.5	0.160	1.952	1.201	3.094	3.0	0.177	2.538	3.047					
2.0	0.181	1.839	1.007	3.080	5.0	0.410	2.659	2.986					
2.5	0.063	1.987	0.467	3.064	7.0	0.040	1.680	2.940					
5.0	0.049	1.961	0.401	2.986	10.0	0.035	1.688	2.889					
6.0	0.051	1.929	0.402	2.961	30.0	0.036	1.604	2.774					
10.0	0.057	1.831	0.406	2.889	50.0	0.037	1.574	2.740					
50.0	0.073	1.642	0.410	2.740	90.0	0.039	1.543	2.704					
90.0	0.077	1.602	0.409	2.704									

TABLE 2. Secondary instabilities of transverse rolls with wavenumber $q_c(\gamma)$ at $\epsilon = \epsilon_{in}$ with Floquet vector $\boldsymbol{s}_{in} = (s_x^{in}, s_y^{in})$ for selected values of the inclination angle γ (see § 2.3). C1: OS instability at $\epsilon_{in} = \epsilon_{OS}$ with $\boldsymbol{s}_{in} = (0, s_y^{OS})$ and frequency ω_0. C2: SH instability at $\epsilon_{in} = \epsilon_{SH}$ with $\boldsymbol{s}_{in} = (q_c/2, s_y^{SH})$. C3: codimension-2 data (OS/SH) for $\gamma = \gamma_i$, $(i = 1, 2, 3)$ at $\epsilon_{in} = \epsilon_{OS} = \epsilon_{SH}$ with s_y^{OS}, ω_0 and s_y^{SH}. As always in this paper, $\boldsymbol{s}_{in}$ is given in units of $1/d$ and ω in units of $1/t_v$.

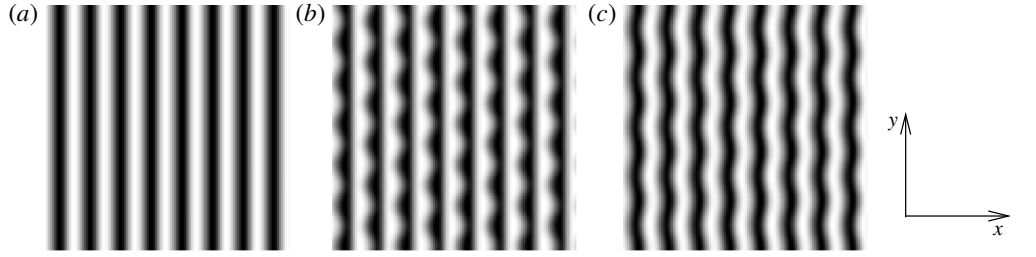

FIGURE 4. Midplane temperature plots in ILC for $L_x = L_y = 8\lambda_c(\gamma)$: (*a*) transverse rolls for $\gamma = 3°$. (*b*) Stationary SH pattern for $\gamma = 1.5°$. (*c*) Snapshot of an OS pattern for $\gamma = 6°$ (for details see text).

space (see (2.9)) using a pseudo-spectral method. The z-dependence of the fields is captured by Galerkin expansions. For the time integration we use the semi-implicit 'exponential time-differencing method' as in Subramanian *et al.* (2016) (for some details see appendix A). The results are typically visualized in this paper by the temperature field at the midplane $z = 0$, i.e. by the function $\theta(x, y, z = 0, t)$. We use individually scaled 8-bit grey scale images, where lighter areas correspond to positive values and darker ones to negative ones. Thus here and in the following a white stripe stands for a roll pair. In figure 4 we show representative stable steady-state snapshots of $\theta(x, y, z = 0, t)$ for different γ calculated with the periodicity lengths $L_x = L_y = 8\lambda_c(\gamma)$. They result from DNS started from random initial conditions after the transients have died out. For $\epsilon < \epsilon_{in}(\gamma)$ with $\gamma > 0°$ we arrive always at stable transverse rolls, as shown in figure 4(*a*). In line with their stability diagram in figure 3 we arrive for $\epsilon > \epsilon_{in}(\gamma)$ either at stationary 3-D SH patterns (see figure 4*b*) or at OS patterns in the form of travelling waves along the y-axis (see a snapshot in figure 4*c*). The frequency ω of the oscillatory patterns is easily obtained by analysing the periodicity in time of $\theta(x, y, z = 0, t)$ at fixed x, y. It should be noted, that our system, as a consequence of the periodic boundary conditions in the plane, is invariant against translations along the x- and the y-directions. Thus using different random initial conditions one arrives at different patterns which, however, can be mapped onto each other by shifting the origin of the coordinate system with respect to x and y.

Inspection of such pictures yields immediately the dominant wavelengths λ_x and λ_y characterizing the spatial periodicity of the patterns in the x–y plane. Note that as a consequence of our periodic boundary conditions in the plane the wavelengths λ_x, λ_y must be integer fractions of L_x and L_y, respectively. In the x-direction all DNS have obviously locked into $\lambda_x = L_x/8 = \lambda_c(\gamma)$, corresponding to 8 roll pairs. The critical wavelength $\lambda_c(\gamma) = 2\pi/q_c(\gamma) \sim 2$ is determined by $q_c(\gamma)$ from table 1 or 2. The theoretical value of λ_c must be reflected in the experimental roll patterns observed in large-aspect-ratio systems, when slowly increasing R until it crosses R_c. Further increasing R should then reveal the secondary instabilities of the rolls as well. This has been indeed confirmed for instance in RBC with $\mathrm{Pr} \approx 1$ (see Bodenschatz *et al.* (2000) and references therein).

The wavelength λ_y has locked into a value $\lambda_y = L_y/m$ with an integer m. Not surprisingly we find in all our simulations that m is chosen by the system such that λ_y is in the vicinity of $\lambda_y^{in} = 2\pi/s_y^{in}$, where the values of s_y^{in} are given in table 2. This selection process has been validated by DNS with different L_y. In general,

https://doi.org/10.1017/jfm.2019.432 Published online by Cambridge University Press

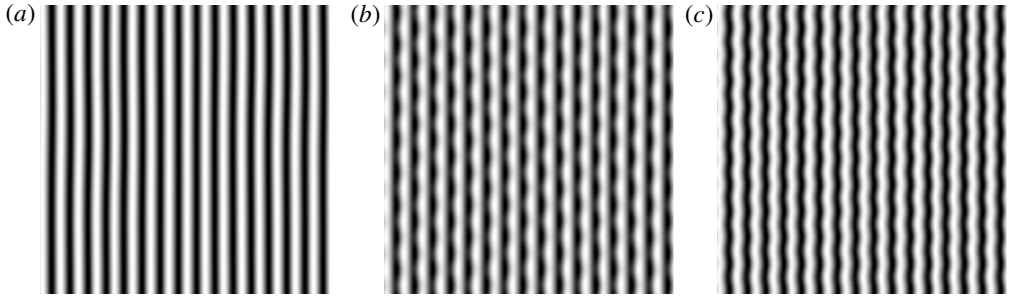

FIGURE 5. Basic patterns as in figure 4 for larger $L_x = L_y = 16\lambda_c(\gamma)$: (*a*) transverse rolls for $\gamma = 50°$, $\epsilon = 0.03$, $\epsilon_0 = -0.8576$ with $\lambda_c = 2.293$. (*b*) SH pattern for $\gamma = 50°$, $\epsilon = 0.045 > 0.037 = \epsilon_{SH}$, $\epsilon_0 = -0.8556$. (*c*) Snapshot of an OS pattern for $\gamma = 5°$, $\epsilon = 0.055 > 0.049 = \epsilon_{OS}$, $\epsilon_0 = -0.2859$ with $\lambda_c = 2.104$ (for details, see text).

larger values of L_y give the system more flexibility in selecting m. Thus we have performed some even more time-consuming simulations for larger periodicity areas in the x–y plane with $L_x = L_y = 16\lambda_c(\gamma)$. As demonstrated in figure 5 we arrive indeed, starting from random initial conditions, at the common basic patterns already shown in figure 4. The SH pattern (see figure 5*b*) for $\gamma = 50°$ has locked into $\lambda_y = L_x/9$, such that $s_y = 2\pi/\lambda_y = 1.541$ matches very well $s_y^{SH} = 1.574$ in table 2. In figure 5(*c*) we show an OS pattern for $\gamma = 5°$, which has locked into $\lambda_y = L_x/11$ corresponding to $s_y = 2.053$ near to $s_y^{OS} = 1.961$ in table 2. Although in this context choosing large values of L_x, L_y would be desirable, this is in general hardly possible in practice due to the fast increase of computer time.

Finally it is obvious that the values of $\boldsymbol{q}_c$ and R_c depend on the real lateral boundary conditions for systems with smaller lateral extensions or different geometries. Typically in analysing experiments one uses thus the experimental value of R_c to calculate the relative distance ϵ (2.12) of R from onset and measures the wave vectors $\boldsymbol{q}$ in units of $|\boldsymbol{q}_c|$. In this way the results obtained via the bifurcation approach match much better the experimental ones.

In the following sections we will discuss the regular SH and OS patterns in more detail.

3.1. *SH patterns*

The SH patterns bifurcate from the transverse rolls for γ in the intervals $1.023° < \gamma < 2.183°$ and $6.169° < \gamma < 90°$. In line with the discussion of the SH instability in § 2.3 their dominant Fourier coefficients belong to the wave vectors $\pm\boldsymbol{q}_i$, $i = 1, 2, 3$ in Fourier space where $\boldsymbol{q}_1 = (q_c, 0)$, $\boldsymbol{q}_{2,3} = (q_c/2, \pm s_y)$, with $s_y \approx s_y^{SH}$ given in table 2. In figure 6 we show for three values of $\gamma = 1.5°$, $50°$, $90°$ representative examples of the time independent midplane temperature field $\theta(x, y)$ in (3.1), where we used $L_x = L_y = 8\lambda_c(\gamma)$. The subharmonic nature of the patterns, where the teeth are shifted by $\lambda_y/2$ after moving by $\lambda_c(\gamma)$ in the x-direction is obvious. In all our simulations the teeth of the SH patterns have pointed to the right for $1.023° < \gamma < 2.183°$ opposite to their orientation for $6.169° < \gamma < 90°$.

In the following we discuss the 3-D character of the SH patterns in more detail using $\gamma = 10°$ and $\epsilon = 0.05$ as a representative example. All pictures have been produced with Mathematica. First we show a 3-D contour plot of the temperature

https://doi.org/10.1017/jfm.2019.432 Published online by Cambridge University Press

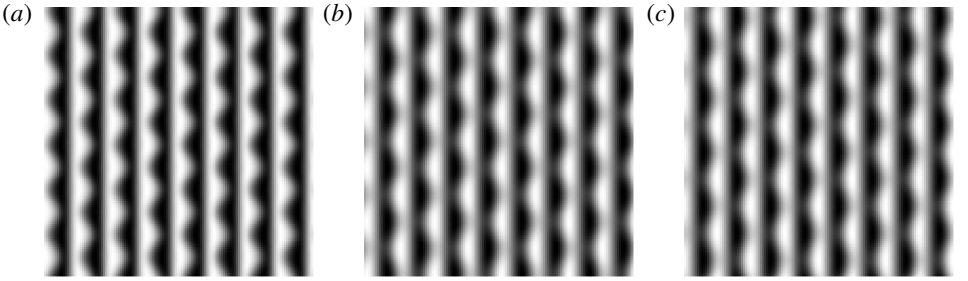

FIGURE 6. Temperature plots of SH patterns for $Pr = 0.025$ and different γ: (*a*) $\gamma = 1.5°$, $\epsilon = 0.12$, $\epsilon_0 = 0.0522$, (*b*) $\gamma = 50°$, $\epsilon = 0.05$, $\epsilon_0 = -0.85487$, (*c*) $\gamma = 90°$, $\epsilon = 0.06$, $\epsilon_0 = -0.88128$.

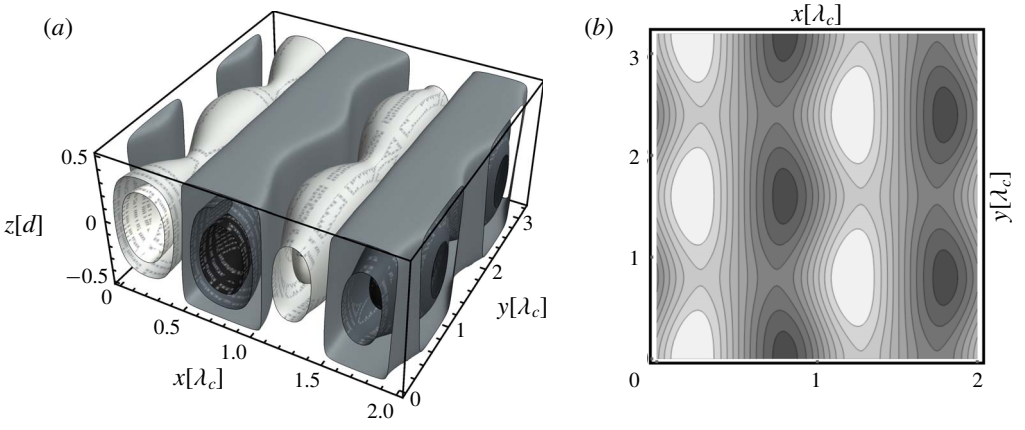

FIGURE 7. DNS for $\gamma = 10°$, $\epsilon = 0.05$, $\epsilon_0 = -0.522145$, $\lambda_x = \lambda_c(\gamma) = 2.175d$ with the periodicity lengths $L_x = L_y = 8\lambda_x$: (*a*) 3-D contour plot of $\theta(x, y, z)$ for $0 \leqq x \leqq 2\lambda_x$, $0 \leqq y \leqq 2\lambda_y = 2(8/5)\lambda_x$; (*b*) 2-D contour plot of the midplane temperature $\theta(x, y, z = 0)$ from panel (*a*).

field $\theta(x, y, z)$ in figure 7, according to which the SH instability leads to a y-periodic bulging out of the original transverse rolls. In figures 7(*b*) and 8(*a*) we show the corresponding 2-D plots of $\theta(x, y, z = 0)$ at the midplane and of $\theta(x, y = 0, z)$ in the x–z-plane at $y = 0$. Due to the subharmonic character of the bifurcation the spatial periodicity of the pattern in x corresponds to the wavelength $2\lambda_c(\gamma)$.

The velocity field (see (2.4)) is much more complex and we have been unable to produce appealing 3-D plots. So we show in figure 8(*b*) a streamplot of (v_x, v_z) obtained from (2.4) in the x–z plane. According to figure 8(*a*) we expect a buoyancy driven upward flow at $x = 1/4$, where θ is maximal at $z = 0$ and analogously a downward flow at $x = 3/4$. This applies analogously to $x = 1.25$ and $x = 1.75$. For standard RBC the flow would be y-independent and parallel to the z-axis at those x values between $z = 1/2$ and $z = -1/2$. In contrast, the streamlines turn here towards the x-direction and develop even small vortices. The additional temperature variations in the x–y-plane (see figure 7*b*) drive also a flow with $v_y \neq 0$. This is documented by the (v_x, v_y) streamlines in figure 9(*a*). The clearly visible vortices are immediately identified by the contour plot of the vertical vorticity $(\nabla \times \boldsymbol{v})_z$ in figure 9(*b*). Note

https://doi.org/10.1017/jfm.2019.432 Published online by Cambridge University Press

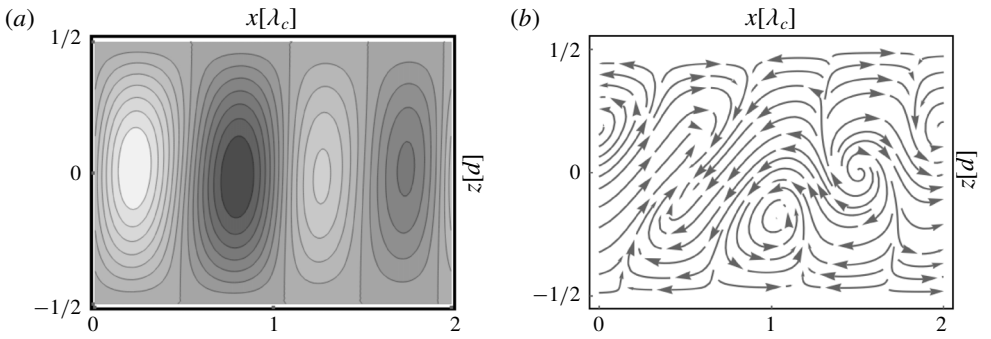

FIGURE 8. Same parameters as in figure 7: (*a*) 2-D contour plot of the temperature field $\theta(x, y = 0, z)$ at $y = 0$ from figure 7(*a*). (*b*) Corresponding streamplot of the velocity components $v_x(x, y = 0, z)$, $v_z(x, y = 0, z)$ (see (2.4)) at $y = 0$.

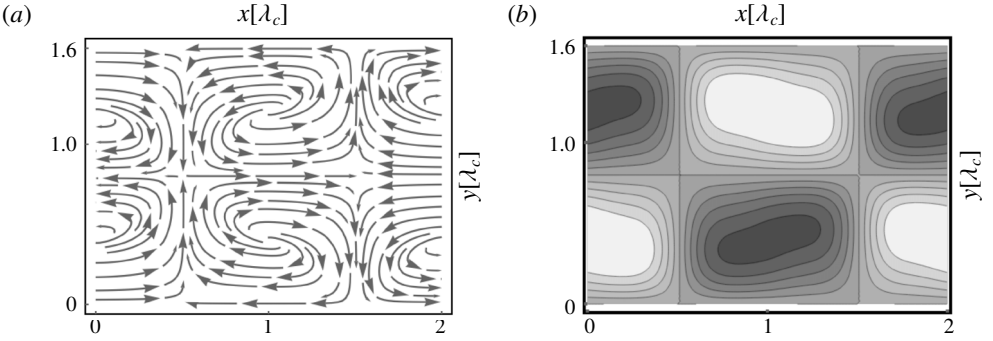

FIGURE 9. Same parameters as in figure 7: (*a*) streamplot of the velocity components $v_x(x, y, z = 0)$, $v_z(x, y, z = 0)$ (see (2.4)) in the midplane $z = 0$. (*b*) The z component of the vorticity, $(\nabla \times \boldsymbol{v})_z$, with $\boldsymbol{v}$ from panel (*a*).

that the subharmonic nature of the bifurcation is here also reflected in the difference between the velocity vector field in the intervals $0 < x < \lambda_x$ and $\lambda_x < x < 2\lambda_x$ and also in a small opposite rotation about the z-axis of the white and black 'lenses' in the vorticity plot.

In the following we will demonstrate that the temperature field $\theta(x, y, z = 0)$ at the midplane shown in figure 7(*b*) is very useful to characterize the SH pattern in more detail. Our starting point is the 2-D Fourier representation of $\theta(x, y, z = 0)$ where the Fourier coefficents with wavevectors $\boldsymbol{q}_1 = (q_c, 0)$ (for the transverse rolls) and $\boldsymbol{q}_{2,3} = (q_c/2, \pm s_y)$ with $s_y \approx s_y^{SH}$ (characterizing the SH instability), are dominant according to § 2.3. In fact, when calculating $\theta(x, y, z = 0)$ using only this wave vector subset, one obtains a function $h(x, y)$, which yields a very useful and accurate approximation of $\theta(x, y, z = 0)$: a plot of $h(x, y)$ looks practically identical to figure 7(*b*) for not too large ϵ.

The phases of the Fourier coefficients associated with the wave vectors $\boldsymbol{q}_{1,2,3}$ defined above fulfil always a special relation detailed in § B.1, which we use as the general signature of SH patterns. As a consequence the function $h(x, y)$, after a suitable shift of the x, y-coordinate system can be always written in a form which depends only on

https://doi.org/10.1017/jfm.2019.432 Published online by Cambridge University Press

Subharmonic patterns					Travelling waves							
γ (deg.)	ϵ	s_y	A_0	B_0	γ (deg.)	ϵ	s_y	ω	ω_0	A_0	B_0	D_0
1.5	0.12	1.900	35.1	6.69	0	0.108	2.171	1.393	1.394	67.8	9.16	0
1.5	0.12	2.100	29.4	9.31	0	0.108	2.190	1.400	1.394	67.6	9.35	0
1.5	0.12	2.241	26.7	10.6	**0**	0.108	2.337	1.482	1.394	68.4	7.29	0
1.5	0.12	2.300	25.9	11.2	0	0.127	2.083	1.354	1.394	67.2	24.4	0
1.5	0.12	2.320	25.7	11.2	0	0.127	2.171	1.395	1.394	67.6	22.5	0
10	0.05	1.400	4.14	1.21	0	0.127	2.181	1.386	1.394	66.7	23.0	0
10	0.05	1.688	3.81	1.70	0	0.127	2.224	1.402	1.394	66.7	22.3	0
10	0.05	1.700	3.73	1.69	0	0.127	2.259	1.417	1.394	66.7	21.8	0
10	0.05	1.810	3.80	1.66	**0**	0.127	2.337	1.454	1.394	67.0	20.5	0
10	0.05	2.000	4.40	0.91	**0.5**	0.130	1.946	1.313	1.376	68.8	22.0	0.30
30	0.05	1.400	1.61	0.52	0.5	0.130	2.147	1.373	1.376	67.3	20.0	0.29
30	0.05	1.604	1.56	0.59	**4**	0.060	1.884	0.392	0.403	8.89	2.54	0.67
30	0.05	1.700	1.57	0.60	4	0.060	1.992	0.398	0.403	8.80	2.47	0.69
30	0.05	1.730	1.58	0.59	4	0.060	2.035	0.399	0.403	8.74	2.46	0.68
30	0.05	2.000	1.80	0.34	**5**	0.055	1.866	0.393	0.401	7.70	1.53	0.39
50	0.05	1.300	1.15	0.28	5	0.055	1.961	0.398	0.401	7.65	1.52	0.40
50	0.05	1.574	1.08	0.38	5	0.055	2.053	0.405	0.401	7.68	1.41	0.39
50	0.05	1.600	1.08	0.38	**5**	0.060	1.866	0.392	0.401	7.60	2.18	0.56
50	0.05	1.710	1.10	0.37	5	0.060	1.961	0.396	0.401	7.59	2.08	0.55
50	0.05	1.900	1.18	0.29	**6**	0.070	1.850	0.386	0.402	6.71	2.59	0.64
90	0.05	1.300	0.92	0.22	6	0.070	1.929	0.393	0.402	6.69	2.49	0.64
90	0.05	1.543	0.87	0.28								
90	0.05	1.600	0.88	0.28								
90	0.05	1.690	0.89	0.27								
90	0.05	1.900	0.97	0.18								

TABLE 3. Left table: amplitudes A_0, B_0 of SH-patterns (see (3.1)) for different γ, ϵ and s_y in the DNS. Near the bold/underlined γ values with the corresponding wavenumbers s_y the amplitudes B_0 are maximal (for details see text). Right table: the analogous data for travelling waves; in addition their frequency ω is listed in comparison with ω_0 at the onset of the OS instability (see table 2).

two real amplitudes $A_0 > 0$, $B_0 > 0$,

$$h(x, y) = A_0 \cos(q_c x) + B_0 \cos(s_y y) \cos(q_c x/2 + \mathfrak{a}\,\pi/4), \quad \text{with } \mathfrak{a} = \pm 1. \tag{3.1}$$

There is a discrete symmetry breaking involved; for $\mathfrak{a} = -1$ the 'teeth' point to the right as in the figure 4(*b*) and for $\mathfrak{a} = 1$ to the left.

The SH solutions exist for $\epsilon > \epsilon_{SH}$ (see table 2). The amplitude B_0 depends on γ and rises continuously with increasing $\epsilon - \epsilon_{SH}$, while for $0 < \epsilon < \epsilon_{SH}$ we have simple transverse rolls with $B_0 = 0$ and $A_0 \propto \sqrt{\epsilon}$. Some characteristic data of our DNS have been collected in table 3 for different γ, where always $L_x = 8\lambda_c(\gamma)$ was chosen. In contrast, we have used different periodicity lengths L_y in the DNS, which then have locked into different values of the wavelength $\lambda_y = L_y/m$, i.e. of the wavenumber $s_y = 2\pi/\lambda_y$ (see table 3). Here for each γ two data sets have been emphasized: the first set (γ in bold) corresponds to DNS with our standard choice $L_y = L_x$ while in the second

https://doi.org/10.1017/jfm.2019.432 Published online by Cambridge University Press

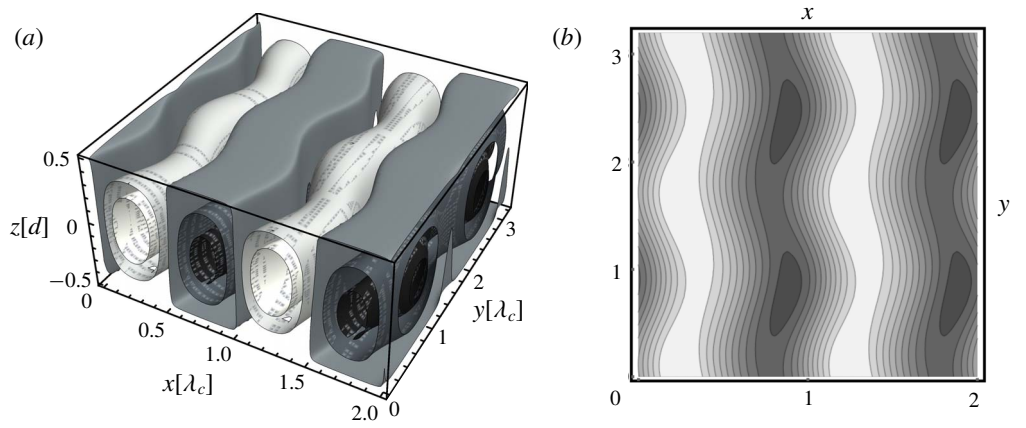

FIGURE 10. DNS for $\gamma = 6°$, $\epsilon = 0.07$, $\epsilon_0 = -0.33836$, $\lambda_x = \lambda_c(\gamma) = 2.175d$ with the periodicity lengths $L_x = L_y = 8\lambda_x$: (*a*) snapshot of a 3-D contour plot of the temperature $\theta(x, y, z)$ for $0 \leqq x \leqq 2\lambda_x$, $0 \leqq y \leqq 2\lambda_y = 2(8/5)\lambda_c$ and $-d/2 < z < d/2$; (*b*) 2-D contour plot of $\theta(x, y, z)$ obtained from panel (*a*) for $y = 0$.

one (γ underlined) values of L_y, slightly different from L_x, have been chosen, such that $s_y = s_y^{SH}$. In vicinity of these s_y values the amplitude B_0 is found to be maximal, which means that the secondary SH instability is most effective.

3.2. *OS patterns*

In our DNS, starting from random initial conditions, we arrive eventually always at stable travelling-wave patterns. In figure 4(*c*) we have shown a representative snapshot for $\gamma = 6°$ at $\epsilon = 0.058$ which originates from the oscillatory instability at $\epsilon_{OS} = 0.051$ with $s_y^{OS} = 1.929$ and $\omega_0 = 0.402$ (see table 2). The simulations have locked into $\lambda_y = 8/5\lambda_c$, i.e. into $s_y = 1.850$, with $\omega = 0.4002$, which is near ω_0. In general, we are confronted in our DNS with very long transients often of the order of $1000t_v$ or more. During that time interval the oscillatory patterns resemble, however, standing-wave ones, to which we return later in this section.

Our basic equations are invariant against the reflection $y \to -y$. This symmetry is spontaneously broken in travelling-wave patterns which move either upwards along y with a phase velocity v_{phas} or downwards with $-v_{phas}$. When transforming the basic equations with $y \to y - (+)v_{phas}t$ for the first (second) case into the comoving frame, the resulting DNS produce essentially equivalent stationary patterns. According to the 3-D contour plot of $\theta(x, y, z)$ in figure 10(*a*) we deal again with deformed convection rolls. In contrast to the SH patterns they bulge out symmetrically to the left and to the right along the x direction when moving along y. The wavelength λ_x is given as $\lambda_c(\gamma)$, while $\lambda_y = 8/5\lambda_x$ holds as evident from the plot of θ in the x–y plane in figure 10(*b*). We leave out a detailed discussion of the velocity field shown in figures 11 and 12 since one finds only quantitative differences compared to the SH patterns in the previous section.

In analogy to the discussion of the SH patterns before, it is very useful to approximate the midplane temperature field $\theta(x, y, z = 0, t)$ by a function $h(x, y, t)$ (see § B.2). That is based on the leading Fourier coefficients with the wave vectors $\boldsymbol{q}_1 = (q_c, 0)$, $\boldsymbol{q}_{2,3} = (q_c, \pm s_y)$ describing the basic transverse rolls ($\boldsymbol{q}_1$) and their

https://doi.org/10.1017/jfm.2019.432 Published online by Cambridge University Press

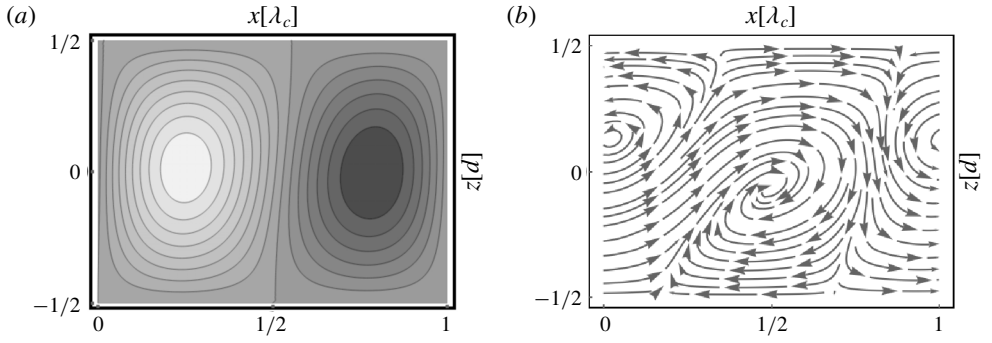

FIGURE 11. Same parameters as in figure 10: (*a*) 2-D contour plot of the temperature field $\theta(x, y=0, z)$ at $y=0$ from figure 10(*a*). (*b*) Corresponding streamplot of the velocity components $v_x(x, y=0, z)$, $v_z(x, y=0, z)$ (see (2.4)) at $y=0$.

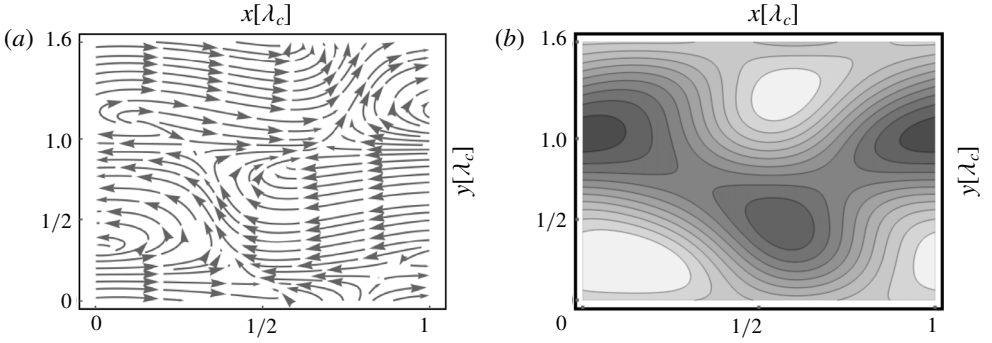

FIGURE 12. Same parameters as in figure 10: (*a*) streamplot of the velocity components $v_x(x, y, z=0)$, $v_z(x, y, z=0)$ (see (2.4)) in the midplane $z=0$. (*b*) The z component of the vorticity, $(\nabla \times \boldsymbol{v})_z$, for $\boldsymbol{v}$ in panel (*a*).

destabilizing oscillatory modes ($\boldsymbol{q}_{2,3}$). In addition the Fourier coefficient with wave vector $\boldsymbol{q}_4 = (0, s_y)$ is also of interest. Exploiting certain relations between the phases of these Fourier coefficients (see § B.2) one arrives finally at

$$h(x, y, t) = A_0 \cos(q_c x) + B_0 \sin(q_c x) \cos[s_y(y - v_{phas} t)] + D_0 \cos[s_y(y - v_{phas} t) + \psi_C], \tag{3.2}$$

with the phase velocity $v_{phas} = \omega / s_y$. The amplitudes A_0, B_0, D_0 obtained in our various DNS with different γ and ϵ are listed in table 3; in addition one finds there the frequency ω of the travelling waves together with the corresponding ω_0 at the onset of the OS-instability (see table 2). The amplitude D_0, always considerably smaller than A_0, B_0, vanishes for $\gamma = 0°$ and describes a x-independent contribution to $h(x, y, t)$ which is, however, practically not visible in DNS snapshots. Inspection of (3.2) shows that D_0 lifts the reflection symmetry $y \to -y$ in the comoving frame ($v_{phas} = 0$) due to the constant positive phase shift $\psi_C = \pi/4(1 + \delta\psi_C)$ with a positive $\delta\psi < 0.05$. The representation of the downwards travelling waves is obtained from (3.2) by the transformations $v_{phas} \to -v_{phas}$ and $\delta\psi_C \to -\delta\psi_c$.

Oscillatory standing-wave patterns appear typically when starting our DNS using restricted initial conditions (see appendix A). A representative time sequence is

https://doi.org/10.1017/jfm.2019.432 Published online by Cambridge University Press

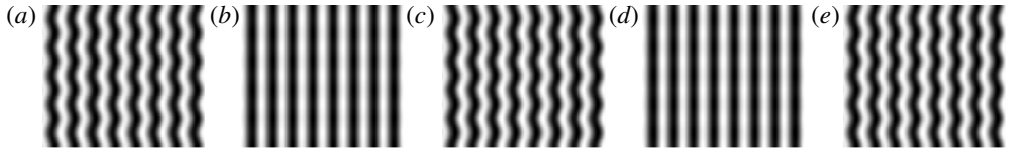

FIGURE 13. Time evolution of standing waves over one time period $T = 16.0t_v$, i.e. with $\omega = 2\pi/T = 0.39237$ again for $\gamma = 6°$, $\epsilon = 0.07$, $\epsilon_0 = -0.33836$.

shown in figure 13, where the sidewise distortion amplitude of the rolls varies in time periodically between a maximum and a minimum. The corresponding function $h(x, y, t)$ for standing waves (see appendix B) reads as follows:

$$h(x, y, t) = A(t)\cos(q_c x) + B(t)\sin(q_c x)\cos(s_y y) + D(t)\cos(s_y y); \tag{3.3a}$$

$$A(t) = A_0 + A_1\cos(2\omega t - \alpha), \quad B(t) = B_0\cos(\omega t), \quad D(t) = D_0\cos(\omega t - \beta). \tag{3.3b–d}$$

The amplitude factors A_1 and D_0 (zero at $\gamma = 0°$) are small and are practically not visible in the DNS snapshots of $h(x, y, t)$. For the representative example, $\gamma = 6°$ and $\epsilon = 0.07$, our DNS were characterized by $\omega = 0.39237$, $A_0 = 6.80$, $A_1 = 0.15$, $\alpha = 2.86$, $B_0 = 3.58$, $D_0 = 0.90$, $\beta = 0.71$. As already mentioned, the standing waves were, however, never stable and developed after superimposing arbitrary noise onto travelling waves.

In the planar case, $\gamma = 0°$, we have compared our DNS with a previous one in the literature (Meneguzzi *et al.* 1987), which was performed for a small-aspect-ratio system (!) at $\epsilon = 0.127$, where $L_x = \lambda_c = 2\pi/q_c = 2.016$ and $L_y = 2\pi/s_y = 2.79$ for $s_y = 2.5$. According to figure 10 in this paper the frequency of the resulting standing wave was approximately $\omega = 1.6$. For comparison we have performed a DNS with restricted initial conditions using a larger aspect ratio with $L_x = 8\lambda_c$ and $L_y = 6(2\pi/s_y) = 0.935L_x$ and also obtained $\omega = 1.6$, which is, however, larger than $\omega_0(\gamma = 0°) = 1.394$ in table 2. However, this pattern was not stable, when continuing the DNS after superimposing arbitrary noise. We arrived at a travelling-wave pattern with a much smaller $s_y = 2.083$, which compares well with $s_y^{OS} = 2.172$. Also the frequency $\omega = 1.35$ fits much better $\omega_0(s_y) = 1.394$.

Note, that in the literature for $\gamma = 0°$ also the less realistic free-slip boundary conditions with respect to the velocity field have been applied (see e.g. Mishra, Wahi & Verma 2010; Dan *et al.* 2017). Though in this way the numerics is considerably simplified, one should be aware of profound qualitative differences to rigid boundary conditions in particular with respect to the vertical vorticity (Clever & Busse 1974).

The following § 4 is devoted to some complex patterns to be found near the codimension-2 points or at larger ϵ.

4. DNS of complex patterns

In the previous section we have described the OS and the SH patterns for γ away from the codimension-2 points. In their vicinity the patterns should show a tendency to become more complex, as indeed demonstrated in § 4.1 on the basis of some characteristic examples. In addition we expect more complicated patterns at larger ϵ, which is confirmed in § 4.2.

4.1. *Patterns in the vicinity of the codimension-2 points*

According to figure 3 and table 2 the first codimension-2 point appears at $\gamma_1 = 1.023°$ with $\epsilon_{OS} = \epsilon_{SH} = 0.133$, where $\lambda_c(\gamma_1) = 2.083$. However, our DNS at a larger $\epsilon =$

https://doi.org/10.1017/jfm.2019.432 Published online by Cambridge University Press

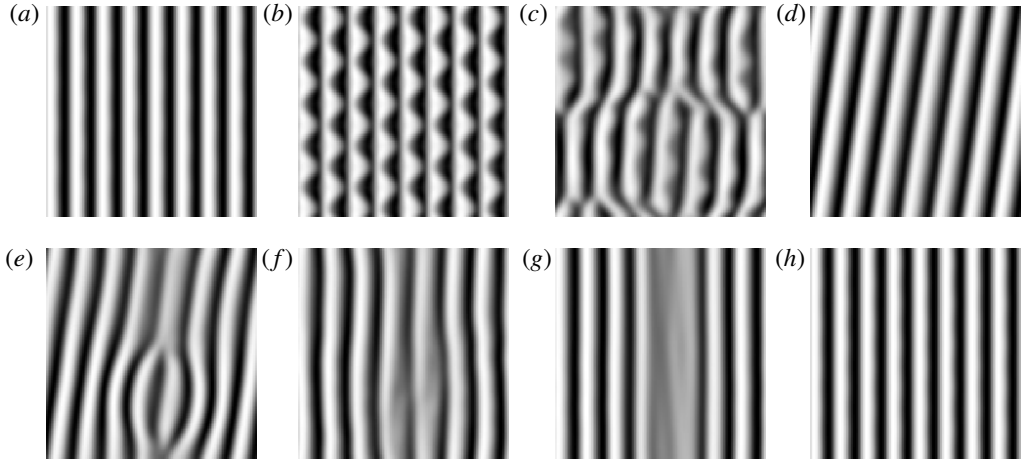

FIGURE 14. Heteroclinic cycle with subharmonic, transverse and oblique patterns from a DNS at $\gamma = 1.5°$ with $L_x = L_y = 8\lambda_c(\gamma)$ at $\epsilon = 0.165$ ($\epsilon_0 = 0.0945$). The pictures are sorted with increasing time t from left to right and top to bottom and correspond to $t = 0$ (*a*), 68 (*b*), 195 (*c*), 278 (*d*), 702 (*e*), 755 (*f*), 788 (*g*), 873 (*h*) in units of t_v.

0.14 for $L_x = L_y = 8\lambda_c(\gamma_1)$ have always produced travelling waves with wavelengths $\lambda_x = \lambda_c$ and $\lambda_y = L_y/5 = 3.237$ where $s_y = 2\pi/\lambda_y = 1.94$ differs not too much from $s_y^{OS} = 2.070$. In contrast, the frequency $\omega = 1.26$ is not well approximated by $\omega_0 = 1.314$. There was no trace of the competing SH instability, maybe because $s_y^{SH} = 1.672$ deviates too much from s_y^{OS}. These general features remain robust, when increasing the horizontal size of the system to $L_x = L_y = 16\lambda_c(\gamma_1)$ using 256×256 Fourier modes in the x–y plane. The system produces again an OS pattern with $\lambda_x = \lambda_c$ but a smaller $\lambda_y = L_y/11 = 2.843$ where $s_y = 2.14 > s_y^{OS}$. The frequency $\omega = 1.35$ was now larger than ω_0.

An analogous scenario was observed at the codimension-2 point $\gamma_2 = 2.183°$ where $\epsilon_{SH} = \epsilon_{OS} = 0.117$ (see table 2) and $\lambda_c(\gamma_2) = 2.044$. Here the DNS have always produced at $\epsilon = 0.125$ with $L_x = L_y = 8\lambda_c(\gamma_2)$ perfect SH patterns without any trace of OS motifs. The DNS have locked into $\lambda_x = \lambda_c(\gamma)_2 = 2.043$ and $\lambda_y = (8/6)\lambda_x$, which corresponds to $s_y = 2.306$ considerably different from $s_y^{SH} = 2.468$. For larger $L_x = L_y = 16\lambda_c(\gamma_2)$ and again with $\epsilon = 0.125$ the DNS had more freedom and locked into $\lambda_y = 16/13\lambda_c$ corresponding to $s_y = 2.496$ much nearer to s_y^{SH}. The fact that $s_y^{OS} = 1.898$ is considerably smaller than the s_y values selected in the DNS, might explain why the competing OS instability has played no role.

Inspection of table 2 shows immediately that s_y^{OS} monotonically decreases with γ while s_y^{SH} increases as long $\gamma < 5°$. Thus there was the chance that in a DNS for γ between γ_1 and γ_2 both stationary SH- and oscillatory motifs might appear. That was indeed the case: in a DNS at $\gamma = 1.5°$ for $L_x = L_y = 8\lambda_c(\gamma_2)$ with $\lambda_c(\gamma_2) = 2.03$ and for $\epsilon = 0.165$ slightly larger than the ϵ_{in} of both the SH and OS instabilities we found a persistent heteroclinic cycle as shown in figure 14. One starts with a transverse roll pattern with 8 roll pairs, which first transforms into a SH pattern. Later we find a pattern with 7 oblique roll pairs which first become transverse, before the original 8 roll pair pattern is recovered. This scheme repeats itself every $873t_v$. We concentrate on SH-type pictures in figure 14 and the corresponding Fourier modes with wave

https://doi.org/10.1017/jfm.2019.432 Published online by Cambridge University Press

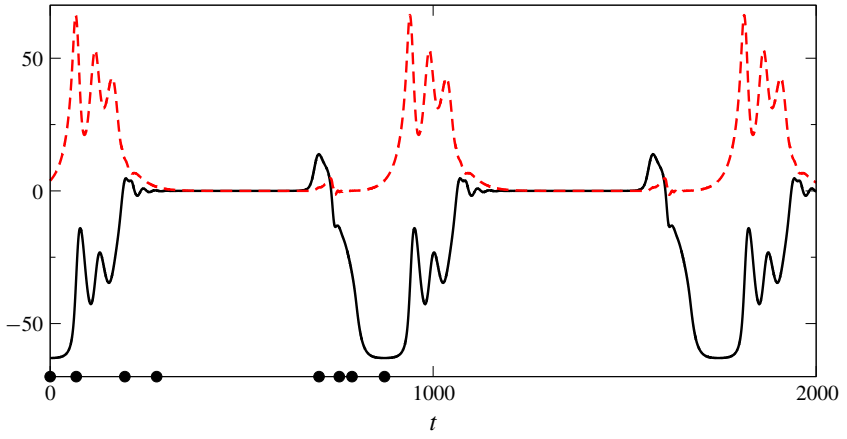

FIGURE 15. (Colour online) Coefficients $A_0(t)$ (solid line) and $3B_0(t)$ (dashed line) in (3.1) as a function of time (in units of t_v) for the heteroclinic cycle in figure 14. The black bullets correspond to the times of the images shown there.

vectors $\boldsymbol{q}_{1,2,3}$ which describe, according to (3.1), a SH pattern. Thus generalizing the representation of stationary SH patterns in (3.1) (see also § B.1) we use the time-dependent amplitudes $A_0(t)$, $B_0(t)$ shown in figure 15 to describe the SH motifs in figure 14. The times t, at which the pictures are presented in figure 14, are marked with the black bullets on the time axis of the figure 15. For the perfect transverse roll pattern at $t = 0$ the amplitude A_0 is maximal, while $B_0 = 0$. Then A_0 decreases and B_0 grows for the following SH pattern. Afterwards both A_0, B_0 essentially become zero for the oblique roll patterns, before the transverse rolls appear again. It took approximately $10\,000t_v$ for the cycle to become stable and we followed it over 15 cycles in our simulation.

Finally, we address the codimension-2 point at $\gamma_3 = 6.169°$ for $\epsilon = 0.051$, where a SH instability with $s_y = 1.62$ competes with an OS instability with $s_y = 1.92$. A simulation with $\epsilon = 0.08$ led to a weakly chaotic sequence of patterns, which are shown in figure 16. It took approximately $10\,000t_v$ in our DNS before that characteristic pattern sequence appeared for the first time, which then persisted afterwards. However, the time lapse between the reappearance of the transverse roll pattern was not constant and varied between $1000t_v$ and $1600t_v$.

However, for the larger aspect ratio $L_x = L_y = 20\lambda_c(\gamma_3)$ with otherwise the same parameters as before, we observed a different scenario. One finds a kind of domain chaos as exemplified by the three snapshots in figure 17 taken at increasing times. The pictures show a background of transverse rolls superseded by SH patches and some dislocations, whose locations change with time.

4.2. *Complex patterns at larger* ϵ

In this section we discuss two very time-consuming simulations, to obtain a first impression of the pattern dynamics for larger ϵ. The first example deals with OS patterns for $\epsilon = 0.172 > \epsilon_{OS} = 0.111$ and for $\gamma = 0.5°$, where the system is slightly anisotropic. The periodicity lengths have been chosen as $L_x = 8\lambda_c(\gamma)$ and $L_y = 5\lambda_y$ with $\lambda_c(\gamma) = 2.018$ and $\lambda_y = (2\pi)/s_y$ where $s_y = s_y^{OS} = 2.147$. First, using restricted random initial conditions (see appendix A) a standing-wave pattern has

https://doi.org/10.1017/jfm.2019.432 Published online by Cambridge University Press

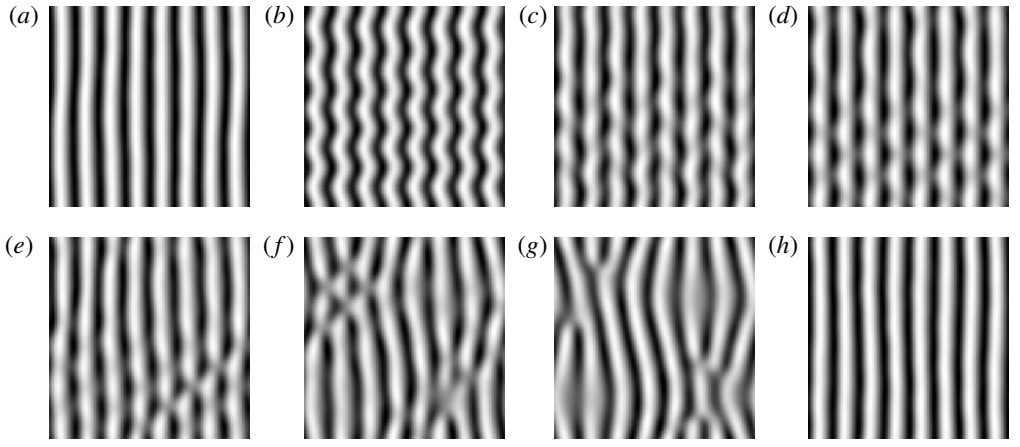

FIGURE 16. Heteroclinic orbit between OS, SH and transverse roll patterns for $\gamma = 6.169°$, $\epsilon = 0.08$ and $\epsilon_0 = -0.3419$ with $L_x = L_y = 8\lambda_c(\gamma)$. The snapshots of $h(x, y, t)$ are shown at times $t = 0$ (*a*), 140 (*b*), 690 (*c*), 890 (*d*), 1130 (*e*), 1300 (*f*), 1360 (*g*), 1490 (*h*) in units of t_v increasing from left to right and from top to bottom.

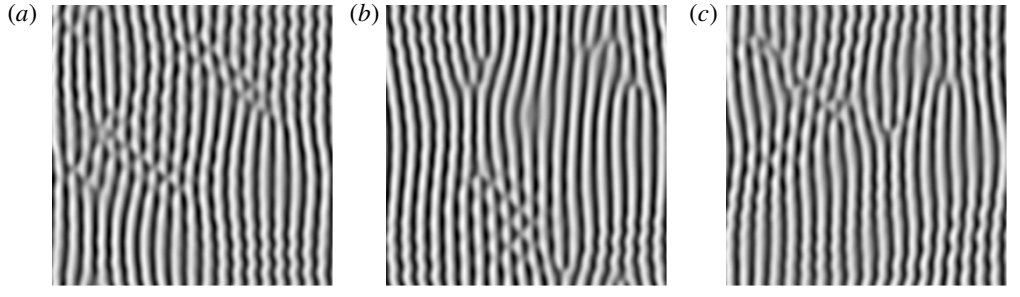

FIGURE 17. Domain chaos in a system with $L_x = L_y = 20\lambda_c(\gamma)$ and the same parameters as in figure 16 ($\gamma = 6.169°$, $\epsilon = 0.08$). Snapshots of the midplane temperature from a DNS started with random initial conditions at consecutive times $t = 3080$ (*a*), 3948 (*b*) and $4198t_v$ (*c*).

been constructed, which was stable after $350t_v$. It is perfectly described by (3.3) with the amplitudes $A_0 = 71.4$, $A_1 = 3.7$, $B_0 = 52.4$. The frequency $\omega = 1.45$ was comparable with $\omega_0 = 1.376$. Then we superimposed noise and continued the run. In figure 18 we show representative snapshots. Their inspection clearly demonstrates that, besides the basic modes $\boldsymbol{q}_{1,2,3}$, additional modes come into play. Nevertheless the contribution of the basic modes is still well described by (3.2) except that we need time-dependent coefficients $A_0(t)$, $B_0(t)$, which are presented in figure 19. They vary periodically in time with a period of approximately $123t_v$ much larger than the fast period $\tau = (2\pi)/\omega = 3.9t_v$, where $\omega = 1.62$ is now considerably larger than the value $\omega = 1.45$ for the standing waves above.

Finally we consider a complex SH-pattern for $\gamma = 50°$ and $\epsilon = 0.15 > \epsilon_{in}^{SH} = 0.05$. Here, according to figure 3(*b*), the transverse rolls are also linearly unstable against oscillatory modes. Inspection of figure 20 shows that these are indeed reflected in the transients of a DNS starting with general random noise. But finally we arrived at a slightly oblique stationary SH-pattern, which was stable.

https://doi.org/10.1017/jfm.2019.432 Published online by Cambridge University Press

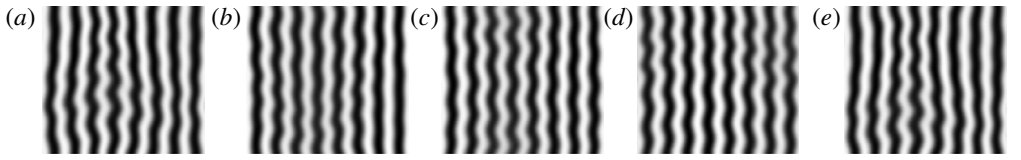

FIGURE 18. Complex travelling-wave pattern for $\gamma = 0.5°$, $\epsilon = 0.172$, $\epsilon_0 = 0.163$, $L_x = 8\lambda_c(\gamma)$, $L_y = 0.906L_x$. The pictures are sorted increasing in time from left to right at $t = 3728$ (*a*), 3741 (*b*), 3779 (*c*), 3804 (*d*), 3851 (*e*) in units of t_v. For the travelling waves we find $\omega = 1.62$.

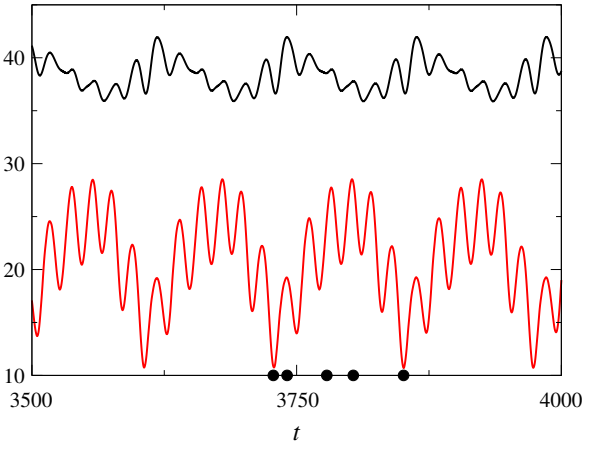

FIGURE 19. (Colour online) Same parameters as in figure 18: the coefficients $A_0(t)/2$ (upper line) and $B_0(t)$ (lower line) in (3.2) as a function of time (in units of t_v). The black bullets correspond to the times of the images in figure 18.

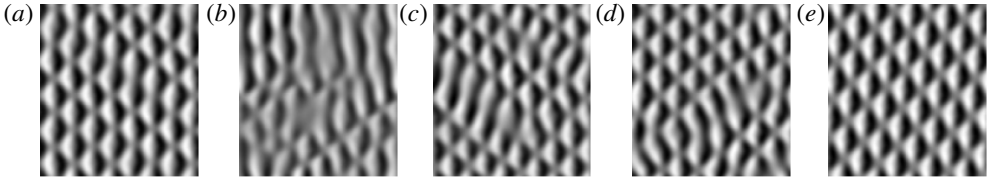

FIGURE 20. Oblique SH pattern for $\gamma = 50°$, $\epsilon = 0.15$, $\epsilon_0 = -0.8410$, $L_x = 8\lambda_c$, $L_y = 1.087L_x$. For the subharmonic pattern we find $s_y = 1.575$. The simulations were started with random noise. The pictures are sorted increasing in time from left to right at $t = 120$ (*a*), 440 (*b*), 1800 (*c*), 2540 (*d*), 4800 (*e*) in units of t_v.

5. Concluding remarks

In this paper we have presented a theoretical analysis of ILC for a low-Prandtl-number fluid (mercury, $Pr = 0.025$), where the fluid layer includes an angle $(90° + \gamma)$ with the gravity vector $\boldsymbol{g}$ (see figure 1). The focus has been on large-aspect-ratio systems with Rayleigh numbers R slightly above the critical values $R_c(\gamma)$ in the spirit of a previous study of ILC with $Pr = 1.07$ (Subramanian *et al.* 2016), where an excellent agreement with the corresponding experiments has been achieved. In

https://doi.org/10.1017/jfm.2019.432 Published online by Cambridge University Press

close analogy to that paper our calculations are based on a bifurcation approach to determine the critical data R_c, $\boldsymbol{q}_c$ and the secondary instabilities of the primary roll patterns. In addition DNS have been used to characterize the pattern evolution.

Inclining the fluid layer breaks isotropy and convection rolls with a definite orientation are seeded at $R = R_c$. For instance, the uniform roll patterns produced at small γ have been used to provide the appropriate initial conditions for experiments at $\gamma = 0°$. This procedure has been shown to be crucial to match the stability diagram of standard, non-inclined RBC with experiments for $Pr \sim 1$ (Cakmur *et al.* 1997).

In general, the pattern types bifurcating at onset and their secondary instabilities vary with γ. For not too small $Pr > 0.264$ (see e.g. Subramanian *et al.* 2016) there exists a codimension-2 angle, γ_{c2}. It separates the regime of longitudinal roll patterns at onset with their axes parallel to the incline from the regime of transverse ones with perpendicular orientation. In particular for $\gamma \approx \gamma_{c2}$ one observes then complex patterns in experiments in agreement with the theory.

Convection in low-Prandtl-number fluids for $\gamma = 0°$ and $R \gtrsim R_c$ has also attracted considerable interest in the past (see e.g. Rossby 1969; Libchaber, Laroche & Fauve 1982; Meneguzzi *et al.* 1987; Clever & Busse 1990; Thual 1992). Here the primary bifurcation is always to transverse rolls for arbitrary γ. However, an oscillatory secondary bifurcation, leading to travelling waves appears already very close to R_c, which has in particular motivated the theoretical studies. It seemed thus natural to investigate low-Prandtl-number ILC for finite γ.

In general, the resulting patterns turned out to be more complex than anticipated. For instance, the secondary bifurcation of the transverse rolls leads either to OS travelling-wave patterns or to 3-D stationary SH ones, which alternate three times with each other already in the fairly small interval $0° \leqslant \gamma \leqslant 6°$. This explains the appearance of complex patterns near the corresponding three codimension-2 points in § 4. In the spirit of an amplitude-equation approach the SH and OS patterns are described by only three leading Fourier modes with a characteristic relation between their phases (see § 3).

For completeness it should be mentioned that a strong sensitivity of the bifurcations at small γ and small $R \gtrsim R_c$ has been also described recently in a theoretical analysis of ILC in binary fluids (Mercader *et al.* 2019). However, this system qualitatively differs from ours: the primary bifurcation of the basic state is typically not continuous and leads to travelling waves already at $\gamma = 0°$ at $R = R_c$. Depending on γ a whole zoo of different pattern types develops, which often are in particular confined to a small part of the fluid layer.

Already decades ago it has also been demonstrated in convection experiments with mercury (Libchaber *et al.* 1982) for $\gamma = 0°$, that an additional magnetic field applied parallel to the fluid layer has an important impact. This has been confirmed in many theoretical studies (see e.g. Busse & Clever 1989) and also continuously extended to the turbulent regime (see e.g. Vogt *et al.* (2018) and references therein). In general, the magnetic field leads to a preferred orientation of the roll axes parallel to the magnetic field. Thus for instance a magnetic field along the incline exerts a kind of torque on the standard transverse rolls for $\gamma \neq 0°$ and small Pr. Thus one expects novel complex convection patterns and their secondary bifurcations in this case already near onset, which we plan to investigate in the near future.

Acknowledgements

The authors are grateful to Professor F. Busse for many valuable discussions and to Professor J. Schumacher for his hints on the most recent publications on low-Prandtl-number convection.

https://doi.org/10.1017/jfm.2019.432 Published online by Cambridge University Press

Appendix A. On the time integration of the OBE

The DNS in this paper is based on a pseudo-spectral code already used in Subramanian *et al.* (2016). Thus according to (2.9) the simulations run in Fourier space on a discrete set of N^2 wave vectors $\boldsymbol{q} = (k\Delta q_x, l\Delta q_y)$ with $-N/2 \leqslant (k, l) \leqslant N/2 - 1$. For the periodicity lengths in this paper we use typically $L_x = L_y = n\lambda_c(\gamma)$ with $n = 8$, 16, 20 and $N = 128$, 256, 320, respectively. In some cases we allow for $L_x \neq L_y$, which implies a corresponding small difference between Δq_x and Δq_y. In this way it is possible to produce periodic patterns with a prescribed wavelength λ_y that match in Fourier space the corresponding Galerkin Floquet vectors $\boldsymbol{s}$ with the y-component $s_y = (2\pi)/\lambda_y$.

For the time integration we use an 'exponential time-differencing method' also described in appendix B1 of Subramanian *et al.* (2016). We found in general time steps of $\mathrm{d}t = 0.002t_v$ to be sufficient to resolve the dynamics of the patterns and to guarantee robust results. In all cases we made sure that the secondary instabilities according to the Galerkin analysis are perfectly reproduced in our DNS. In view of typical transients of $1000t_v$ and more before the patterns would become steady (see e.g. § 3.2), our DNS are in general very time consuming. Using $\kappa = 4.62 \times 10^{-6}$ m^2 s^{-1} for mercury the thermal diffusivity time takes the value $t_v = d^2/\kappa = 21.6$ s for $d = 1$ cm. Thus our DNS needed typically more than 5×10^5 time steps in particular for the OS patterns.

Note, that in view of the periodic boundary conditions, the origin of the coordinate system in the x–y plane can be arbitrarily shifted, when analysing a single run. Thus a shift by $\boldsymbol{x}_0 = (x_0, y_0)$ with arbitrary x_0, y_0 leads to a phase factor $\exp[\mathrm{i}\boldsymbol{x}_0 \cdot \boldsymbol{q}]$ multiplying the original Fourier coefficients $\boldsymbol{V}(\boldsymbol{q}, z, t)$ in (2.9). Consequently the amplitudes A_0, B_0 of the leading Fourier coefficients in (3.1) and in (3.2), (3.3) could be made real.

Usually our simulations have started with general random initial conditions. To save computer time, in particular to construct standing waves, alternatively a kind of restricted initial conditions has been used. First they are based only on the Fourier coefficients with the wave vectors $\boldsymbol{q}_{1,2,3}$ which represent the functions $h(x, y)$ in appendix B. Furthermore the Fourier coefficients had to fulfil the phase restriction in (B 3) and (B 10*d–f*). It was also helpful, for smaller changes of parameters to use already existing results.

Appendix B. Signature of subharmonic and oscillatory patterns in the DNS

A first impression of SH and OS patterns is simply obtained by looking at the corresponding DNS pictures and their time evolution, as done in §§ 3 and 4. In this section we discuss in more detail the SH and OS patterns in terms of the function $h(x, y; t)$ which derives from $\theta(x, y, z; t)$ at the midplane $z = 0$, when keeping only the leading Fourier coefficients. These are directly provided by our pseudo-spectral code and their analysis gives an important clue to analysing SH and OS as discussed in the following subsections.

B.1. *The function $h(x, y, t)$ for SH patterns*

The SH patterns are spanned by the dominant wave vectors $\boldsymbol{q}_1 = (q_c, 0)$ and $\boldsymbol{q}_{2,3} = (q_c/2, \pm s_y)$. Thus $h(x, y)$, the leading approximation of the midplane temperature $\theta(x, y, z = 0)$ introduced in § 3.1 is in general given as

$$h(x, y) = Re\{\exp(\mathrm{i}q_c x)\hat{A} + \exp(\mathrm{i}q_c x/2)(\exp(\mathrm{i}s_y y)\hat{B} + \exp(-\mathrm{i}s_y y)\hat{C})\}, \tag{B 1}$$

$$\hat{A} = |\hat{A}|\exp(\mathrm{i}\phi_A), \quad \hat{B} = |\hat{B}|\exp(\mathrm{i}\phi_B), \quad \hat{C} = |\hat{C}|\exp(\mathrm{i}\phi_C). \tag{B 2a–c}$$

https://doi.org/10.1017/jfm.2019.432 Published online by Cambridge University Press

It turns out that $h(x, y)$ describes a perfect SH pattern when the phases of the Fourier coefficients allow the following representation:

$$\phi_B = \phi_A/2 - \psi + \mathfrak{a}\,\pi/4; \quad \phi_C = \phi_A/2 + \mathfrak{a}\,\pi/4 + \psi, \tag{B 3a,b}$$

with $\mathfrak{a} = \pm 1$ and the phase shift ψ. Obviously (B 3) is equivalent to

$$\phi_B + \phi_C = \phi_A + \mathfrak{a}\pi/2. \tag{B 4}$$

The system is then only characterized by the moduli A_0, B_0 of the Fourier coefficients as follows:

$$|\hat{A}| = A_0, \quad |\hat{B}| = |\hat{C}| = B_0/2. \tag{B 5a,b}$$

The phase shifts ϕ_A and ψ can be put to zero by a shift of the origin of the x, y coordinate system and one arrives at the most simple representation of $h(x, y)$ in (3.1).

We found that the procedure described above works also when a SH pattern appears only for finite time as in figure 14. One arrives then at time-dependent amplitudes $A_0(t), B_0(t)$ as shown in figure 15.

B.2. *The function $h(x, y, t)$ for OS patterns*

The discussion of the OS patterns follows closely the one for SH patterns, though it is slightly more complicated since already the regular OS patterns oscillate in time. The OS patterns are spanned by the dominant wave vectors $\boldsymbol{q}_1 = (q_c, 0)$ and $\boldsymbol{q}_{2,3} = (q_c, \pm s_y)$. In addition it is useful to keep also the mode with wave vector $\boldsymbol{q}_4 = (0, s_y)$ as a small correction.

Thus in analogy to (B 1) we use the following ansatz for $h(x, y, t)$:

$$\begin{aligned} h(x, y, t) \;=\; & Re\,\{\exp[\mathrm{i}q_c x]\,[|\hat{A}(t)|\exp[\mathrm{i}\phi_A] + |\hat{B}(t)|\exp[\mathrm{i}s_y y + \mathrm{i}\phi_B(t)] \\ & + |\hat{C}(t)|\exp[-\mathrm{i}s_y y + \mathrm{i}\phi_C(t)]] + |\hat{D}(t)|\exp[\mathrm{i}s_y y + \mathrm{i}\phi_D(t)]\}\,. \end{aligned} \tag{B 6}$$

For travelling waves the phases of the Fourier coefficients have to fulfil the condition

$$\phi_B = \psi - \omega t + \pi/2 + \phi_A; \quad \phi_C = -\psi + \omega t + \pi/2 + \phi_A, \quad \phi_D = -\omega t + \phi_D^0, \tag{B 7a–c}$$

with the frequency ω. In analogy to (B 4) we arrive at

$$\phi_B + \phi_C = 2\phi_A + \pi. \tag{B 8}$$

The system is then mainly characterized by the moduli A_0, B_0 of the Fourier coefficients as before and in addition by the small correction D_0 as

$$|\hat{A}| = A_0, \quad |\hat{B}| = |\hat{C}| = B_0/2, \quad |\hat{D}| = D_0. \tag{B 9a–c}$$

The amplitude D_0 vanishes at $\gamma = 0°$ and increases then slowly with increasing γ. Again after a suitable shift of the origin of the coordinate system, ϕ_A, and ψ can be put to zero and one arrives for $h(x, y, t)$ in (3.2). The amplitudes A_0, B_0, D_0 are time independent for regular OS patterns as discussed in § 3.2. However, also intermediate travelling-wave patterns as in figure 18 are very well described by time dependent amplitudes $A_0(t)$ and $B_0(t)$ (see figure 19).

https://doi.org/10.1017/jfm.2019.432 Published online by Cambridge University Press

Finally we come to the standing waves, which are represented as the travelling ones in (B 6) excepting some minor modifications in the complex amplitudes as follows:

$$|\hat{A}| = A_0 - A_1\cos(2\omega t + \alpha), \quad |\hat{B}| = |\hat{C}| = B_0/2\cos(\omega t), \quad |\hat{D}| = D_0\cos(\omega t - \beta); \tag{B 10a–c}$$

$$\phi_B = \psi + \pi/2 + \phi_A; \quad \phi_C = -\psi + \pi/2 + \phi_A; \quad \phi_D = \psi. \tag{B 10d–f}$$

Eliminating then ψ, ϕ_A as before yields $h(x, y, t)$ given in (3.3).

REFERENCES

BODENSCHATZ, E., PESCH, W. & AHLERS, G. 2000 Recent developments in Rayleigh–Bénard convection. *Annu. Rev. Fluid Mech.* **32**, 709–778.

BUSSE, F. H. 1989 Fundamentals of thermal convection. In *Mantle Convection: Plate Tectonics and Global Dynamics* (ed. W. H. Peltier). Gordon and Breach.

BUSSE, F. H. & CLEVER, R. M. 1989 Traveling-wave convection in the presence of a horizontal magnetic field. *Phys. Rev.* A **45**, 1954–1961.

BUSSE, F. H. & CLEVER, R. M. 1992 Three-dimensional convection in an inclined layer heated from below. *J. Engng Maths* **26**, 1–49.

BUSSE, F. H. & CLEVER, R. M. 2000 Bursts in inclined layer convection. *Phys. Fluids* **12**, 2137–2140.

CAKMUR, R. V., EGOLF, D. A., PLAPP, B. & BODENSCHATZ, E. 1997 Bistability and competition of spatiotemporal chaotic and fixed point attractors in Rayleigh–Bénard convection. *Phys. Rev. Lett.* **79**, 1853–1856.

CHANDRASEKHAR, S. 1961 *Hydrodynamic and Hydromagnetic Stability*. Clarendon Press.

CLEVER, R. M. & BUSSE, F. H. 1974 Transition to time-dependent convection. *J. Fluid Mech.* **85** (4), 625–645.

CLEVER, R. M. & BUSSE, F. H. 1977 Instabilities of longitudinal convection rolls in an inclined layer. *J. Fluid Mech.* **81** (1), 107–127.

CLEVER, R. M. & BUSSE, F. H. 1990 Convection at very low Prandtl numbers. *Phys. Fluids* A **2** (3), 334–339.

CROSS, M. C. & HOHENBERG, P. C. 1993 Pattern formation outside of equilibrium. *Rev. Mod. Phys.* **65**, 851–1112.

DAN, S., GHOSH, M., NANDUKUMAR, Y., DANA, S. & PAL, P. 2017 Bursting dynamics in Rayleigh–Bénard convection. *Eur. Phys. J.* **226** (9), 2089–2099.

LAPPA, M. 2009 *Thermal Convection, Patterns, Evolution and Stability*. Wiley.

LIBCHABER, A., LAROCHE, C. & FAUVE, S. 1982 Period doubling cascade in mercury, a quantitative measurement. *J. Phys. Lett. Paris* **43** (7), 211–216.

MENEGUZZI, M., SULEM, C., SULEM, P. L. & THUAL, O. 1987 Three-dimensional numerical simulation of convection in low-Prandtl-number fluids. *J. Fluid Mech.* **182**, 169–191.

MERCADER, I., BATISTE, O., ALONSO, A. & KNOBLOCH, E. 2019 Effects of small inclination on binary convection in elongated rectangular cells. *Phys. Rev.* E **99**, 023113.

MISHRA, P. K., WAHI, P. & VERMA, M. K. 2010 Patterns and bifurcations in low–Prandtl-number Rayleigh–Bénard convection. *Europhys. Lett.* **89** (4), 44003.

ROSSBY, H. T. 1969 A study of Bénard convection with and without rotation. *J. Fluid Mech.* **36** (2), 309–335.

SHISHKINA, O. & HORN, S. 2016 Thermal convection in inclined cylindrical containers. *J. Fluid Mech.* **790**, R3.

SUBRAMANIAN, P., BRAUSCH, O., DANIELS, K. E., BODENSCHATZ, E., SCHNEIDER, T. M. & PESCH, W. 2016 Spatio-temporal patterns in inclined layer convection. *J. Fluid Mech.* **794**, 719–745.

TEIMURAZOV, A. & FRICK, P. 2017 Thermal convection of liquid metal in a long inclined cylinder. *Phys. Rev. Fluids* **2**, 113501.

https://doi.org/10.1017/jfm.2019.432 Published online by Cambridge University Press

THUAL, O. 1992 Zero-Prandtl-number convection. *J. Fluid Mech.* **240**, 229–258.

VERMA, M. K. 2018 *Physics of Buoyant Flows*. World Scientific.

VOGT, T., ISHIMI, W., YANAGISAWA, T., TASAKA, Y., SAKURABA, A. & ECKERT, S. 2018 Transition between quasi-two-dimensionsal and three-dimensional Rayleigh-regular flow reversals in Rayleigh–Bénard convection in a horizontal magnetic field. *Phys. Rev. Fluids* **3**, 013503.

https://doi.org/10.1017/jfm.2019.432 Published online by Cambridge University Press